International Journal of Crashworthiness

ISSN: 1358-8265 (Print) 1754-2111 (Online) Journal homepage: www.tandfonline.com/journals/tcrs20

Air cargo container experimental characterisation and finite element modelling under crash related loads

Matthias Waimer, Paul Schatrow, Tobias Behling & Dorothea Schlie

To cite this article: Matthias Waimer, Paul Schatrow, Tobias Behling & Dorothea Schlie (27 Mar 2026): Air cargo container experimental characterisation and finite element modelling under crash related loads, International Journal of Crashworthiness, DOI: 10.1080/13588265.2026.2644158

To link to this article: https://doi.org/10.1080/13588265.2026.2644158

INTERNATIONAL JOURNAL OF CRASHWORTHINESS
https://doi.org/10.1080/13588265.2026.2644158

Taylor & Francis
Taylor & Francis Group

Air cargo container experimental characterisation and finite element modelling under crash related loads

Matthias Waimer, Paul Schatrow, Tobias Behling and Dorothea Schlie

German Aerospace Center (DLR), Institute of Structures and Design, Stuttgart, Germany

ABSTRACT

This article presents experimental results of crash tests performed on air cargo containers, as well as aspects on the finite element modelling for integration of container models in aeroplane crash simulations. Containers of type AKE and AKH were tested and simulated. Following the building block approach, the container structures were tested at different structural scales, while material characterisation at the coupon level was not performed due to sufficient data available from manufacturer data sheets. In total, eight full-scale drop tests of AKE and AKH containers were performed with the force-displacement characteristics as main test result. Finite element models of both container types were developed and validated based on the experimental results. The simulations were performed using the explicit finite element software Abaqus/Explicit. The primary intent of this article is the provision of experimentally determined crash characteristics of air cargo containers that can be used in aeroplane crash analyses.

ARTICLE HISTORY
Received 23 April 2024
Accepted 6 March 2026

KEYWORDS
Crashworthiness; air cargo container; AKE; AKH; experimental testing; finite element simulation

1. Introduction

Transport aeroplane crashworthiness is affected by the cargo loading configuration. Typical transport aeroplane fuselage architectures define a cargo hold below the cabin where passenger's luggage or other cargo is loaded. In case of a crash landing, the lower fuselage shell deforms and the crash loads are transmitted through the fuselage structure to the passengers sitting on their seats. Without cargo loading, these crash loads are transmitted through the lower fuselage side shell and, if installed, through the vertical cabin floor support struts to the cabin floor. When cargo is loaded, the cargo mass may affect the lower fuselage deformation. Furthermore, the deforming lower fuselage may eliminate any clearance between cargo and the cabin floor above, so that the crash loads can be transmitted directly through the cargo to the cabin floor, see Figure 1. This direct crash load path is strongly dependent on the cargo stiffness and showed significant influence on the crash kinematics and passenger loads in crash tests performed in the past [1–5].

Despite the relevance of cargo loading for transport aeroplane crashworthiness, experimental studies on cargo characterisation for crash analyses are rare and only limited information can be found in literature. FAA and NASA performed fuselage section drop tests with fuel tanks or bulk loaded in the cargo hold. In the scope of these studies, luggage crush tests were performed to characterise the crash relevant and non-linear crush stiffness of bulk loading [4,5]. Based on the experimentally determined characteristics, luggage surrogates in terms of foam configurations were installed in the cargo hold of an aeroplane full-scale crash test [6]. Further luggage characterisation was performed in a more systematic approach by investigating the influence of different luggage case material under quasi-static loading rates [7]. The effect of luggage on the crashworthiness of a fuselage section was numerically investigated by different authors and showed significant energy absorption by luggage compression during the crash event [4,8].

However, to the author′s knowledge, there is no information available on the crash characteristics of air cargo containers, which are widely used for cargo loading in wide-body and partly also in single-aisle (Airbus A320) category transport aeroplanes. Drop tests on wide-body fuselage sections equipped with cargo containers were performed in the past [9,10], but details on the container crash behaviour are not reported. Other research work reported in literature is related to explosion-resistant air cargo containers that again provide no information on the container crash characteristics [11].

The lag of experimental data for validation of finite element models of air cargo containers is the motivation of this present study which aims at experimentally characterise representative air cargo containers and provide that experimental data to the research community. Furthermore, the study aims at validate finite element models following the building block approach and provide suggestions on the modelling of air cargo containers.

CONTACT Matthias Waimer matthias.waimer@dlr.de

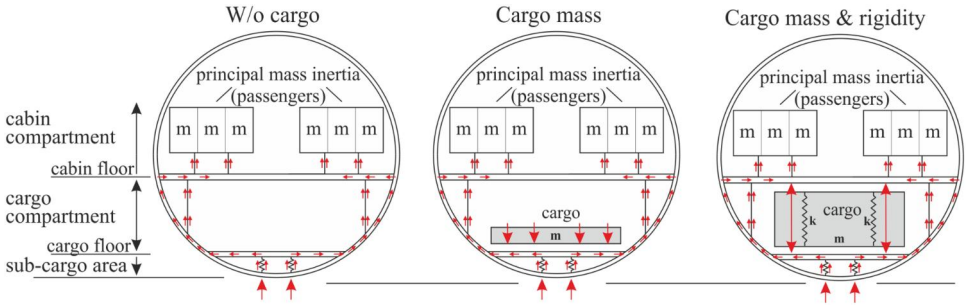

Figure 1. The effect of cargo loading in case of a crash event.

The building block approach is applied in this study and section 2 provides an overview on the selected building block levels and corresponding experimental tests defined for the characterisation of the air cargo containers. The experimental test programme and the results are presented in section 3. The finite element modelling and simulation is discussed in section 4. Conclusions are given in section 5.

2. The building block for experimental characterisation and model validation

The building block approach is a method to gain confidence in designs or analysis methods, working from lower level components to more complex assemblies, using knowledge gained at each step to inform higher fidelity representations [12]. At the end, the finally validated analysis method is capable of representing respectively predicting the entire structure complexity of the considered application. Using simulation models of air cargo containers in aeroplane crash simulations requires this capability to ensure the effects of cargo loading are truthfully represented and hence the aeroplane structure will be well designed for ensuring crashworthiness.

Representative air cargo containers were selected for experimental characterisation at different structural levels. Although different container manufacturers provide their products on the market, most representative air cargo containers used in the current worldwide fleet are of similar design with a framework of aluminium profiles and sheets which are assembled using bolted gussets in each corner of the container. Other designs such as containers fabricated from light-weight composite materials are not considered here.

Used containers were inspected and selected according to the criterion of showing usual wear and tear but being still airworthy. Containers of type LD3 (IATA code: AKE) and LD3-45 (IATA code: AKH) were selected for characterisation of the most widely used container types for wide-body and single-aisle (A320) category transport aeroplanes, which are in detail DRIESSEN LD3 containers and DRIESSEN A320 LD (LD3-45) containers, see Figure 2. ZODIAC AEROSPACE as legal successor of DRIESSEN provided detailed design data for setting up the finite element models.

In total, 13 used air cargo containers were purchased (four containers of type AKH and nine of type AKE) and shipped to DLR.

Two relevant aspects were considered for the test and analysis plan.

First, for the considered AKH and AKE containers the part materials are identical and the part designs are very similar, e.g. profile sections of identical cross-sections as well as identical gusset parts are used. Therefore, all four AKH containers were reserved for full-scale testing and four out of the nine AKE containers were selected for disassembly to extract the test samples for testing at the lower structural levels.

Second, a comprehensive set of material data for the sheets, profiles, gussets, canvas, and bolted joints was provided by the manufacturer. Especially for the aluminium alloys of sheets, profiles, and gussets the material data could be supplemented by existing experimental data from past research work. For this reason, the coupon level tests were initially set as optional and finally skipped as the information from the data sheets was found to be sufficient.

A test plan was developed for characterisation of all relevant container details necessary to validate the finite element models. The building block is depicted in Figure 3.

Element level characterisation considered the container profile sections. Especially the vertical stanchions were expected to collapse and to develop plastic hinges under vertical crash impact loading. Furthermore, deformation of the base profile sections may occur in case of cargo floor distortion under real-world crash conditions. At the element level, three-point bending tests were planned for all relevant container profile sections to provide experimental data of profile section bending and formation of plastic hinges.

Detail level characterisation considered the container assembly which is a bolted connection of profile sections, gussets and sheets. The container roof corners were expected to experience bending loads due to the vertical impact loading of equidistant cabin floor cross beams in a real-world crash event as well as due to potential container distortion. The container base corners were expected to experience mainly crush loads. Accordingly, roof corner bending tests were planned while the base corners were considered for crush testing.

Regarding the given container design, the roof and base corners considered at the detail level can be seen as the highest level for reasonable structural testing of container

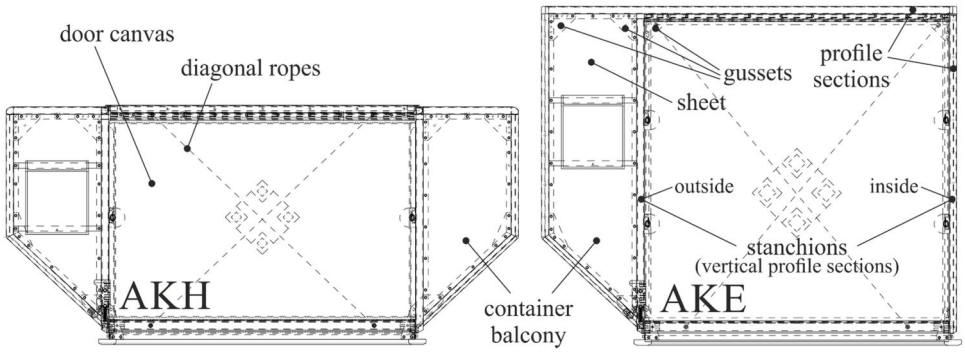

Figure 2. AKH (left) and AKE (right) containers considered in this study.

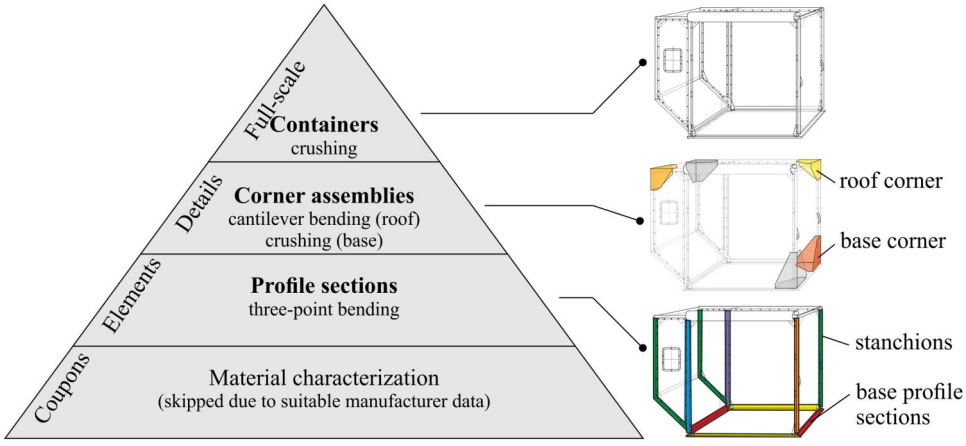

Figure 3. Building block for container characterisation.

sub-assemblies. Hence, the sub-component and component level of a typical building block is not considered here.

At the full-scale level, the AKE and AKH containers were planned to be tested by vertical drop tests. For typical aeroplane crashes, the vertical impact can be seen as the dominant component of a combined horizontal-vertical impact condition as most of the structural deformation of an aeroplane can be attributed to the vertical crash loads. With the number of containers purchased for this research programme, four full-scale tests for each of both container types were performed.

3. Experimental characterisation

In this section, the experimental test campaigns are described and the test results are presented for each building block level.

3.1. Element level testing

At the element level, the container profile sections were tested under three-point bending. The tested profile sections comprise all vertical stanchions of the container as well as the base profile sections, as illustrated in Figure 4(a). Stanchions are installed in a 'filigree' design at the container rear side and a 'massive' design at the container front side. The 'massive' design provides increased wall thickness for reinforcement of the door surround structure.

Quasi-static and transient-dynamic testing was performed, both in a high-speed testing machine Instron VHS PLS100/20M. The test setup is shown in Figure 4(b). The nominal piston velocities were 50 mm/min respectively 2.5 m/s. Three piezo-electric load cells were used for force measurements at both supports (Kistler 9061 A) as well as at the loading stamp (Kistler 9371B). The force results presented in this article are measurements at the loading stamp with a sampling rate of 500 Hz for quasi-static testing and 50,400 Hz for dynamic testing. One high-speed camera of type FASTCAM SA-Z (Photron) recorded the test sequences in a front view position with frame rates of 50 fps for quasi-static testing as well as 50,400 fps for dynamic testing. Force signals were synchronised with the high-speed video camera. The loading stamp displacements were measured by Digital Image Correlation (DIC) using the high-speed video records and the GOM Correlate software. Force signals of the dynamic tests were filtered with a Butterworth filter and a cut-off frequency of 500 Hz, all other results are unfiltered. The number of tests for each profile section varies according to the availability of test specimens from the container disassembly.

Results of all tests, in terms of force-displacement measurements, are presented in Figures 5 and 6. The range of force-displacement response for the different profile sections is exemplarily shown in Figure 7 and highlights strong variations in bending strength and absorbed energy depending on the profile design. The base profile 39127 is installed in the container in two configurations, with and

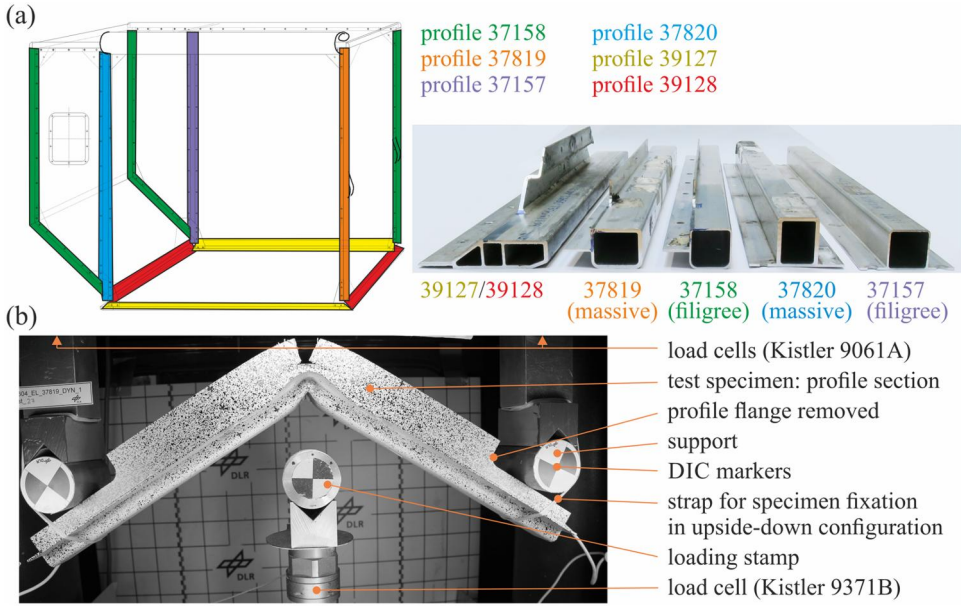

Figure 4. Element level test campaign, (a) tested profile sections, (b) three-point bending test setup.

without flange holes. The results of both configurations show significant differences in the absorbed energy as the flange holes served as crack initiators. Different failure behaviour dependent on the profile design is exemplarily illustrated in Figure 8.

3.2. Detail level testing

At the detail level, the container corner assemblies were tested, see Figure 9(a). The roof corner test specimens were tested under cantilever bending in a 'tension' and 'compression' mode, as illustrated in Figure 9(b). The tension mode applied cantilever bending on the roof corner that led to tensile loading of the gusset and failure of the bolted joints. The compression mode applied cantilever bending that resulted in compression loading of the gusset and buckling respectively instability of the gusset and the profile flanges.

3.2.1. Roof corner testing

As illustrated in Figure 9(a), three different roof corner types were extracted from the containers. Due to symmetry in the AKE container, the roof corners are of identical or mirrored design. This includes identical profile sections, gussets, sheets, and bolted joints. For that reason, all tested roof corners can be evaluated in one data set.

Quasi-static and transient-dynamic testing was performed, both in a high-speed testing machine Instron VHS PLS100/20M. The test setups are shown in Figure 9(b1,b2). The roof corner test specimens were mounted on a fixation plate and loaded by a loading stamp mounted on the machine piston. The nominal piston velocities were 50 mm/min respectively 2.5 m/s. One piezo-electric load cell of type Kistler 9371B was used for force measurements and installed at the loading stamp. The force results presented in this article are measurements at the loading stamp with a sampling rate of 500 Hz for quasi-static testing and 36,000 Hz for dynamic testing. Force signals were synchronised with the high-speed video camera. One high-speed camera of type FASTCAM SA-Z recorded the test sequences in a front view position with frame rates of 50 fps for quasi-static testing as well as 36,000 fps for dynamic testing. The loading stamp displacements were measured by Digital Image Correlation (DIC) using the high-speed video records and the GOM Correlate software. Force signals of the dynamic tests were filtered with a Butterworth filter and a cut-off frequency of 500 Hz, all other results are unfiltered.

Results of all roof corner tests, in terms of force-displacement measurements, are presented Figures 10 and 11.

Representative failure effects under tension mode bending are illustrated in Figure 12 based on an exemplary test curve. Non-linearities in the force-displacement response prior to the onset of damage are caused by bolted joint clearance effects as well as deformation of the profile cross section caused by the tension loads introduced in the profile flange. Clearances in these bolted joints are more prominent as known from aircraft primary structures as air cargo containers are typically delivered in shipsets and hence bolted joint drill holes are placed with broader tolerances already during part manufacturing. Test specimen failure is concentrated on the bolted joints and showed shear-out at the profile flange, with a mixed-mode failure for bolted joint #2, as can exemplarily be seen in Figure 12.

Representative failure effects under compression mode bending are illustrated in Figure 13 based on an exemplary test curve. Again, non-linearities in the force-displacement response can be observed which can be attributed to clearances in the bolted joints and elastic deformation of the profile cross section, but also to buckling of the sheet. The thicker gusset part remained stable at this state which subsequently led to larger profile cross section deformations due to the intrusion of the gusset. With progressing displacement, the deformed profile cross section got in contact with

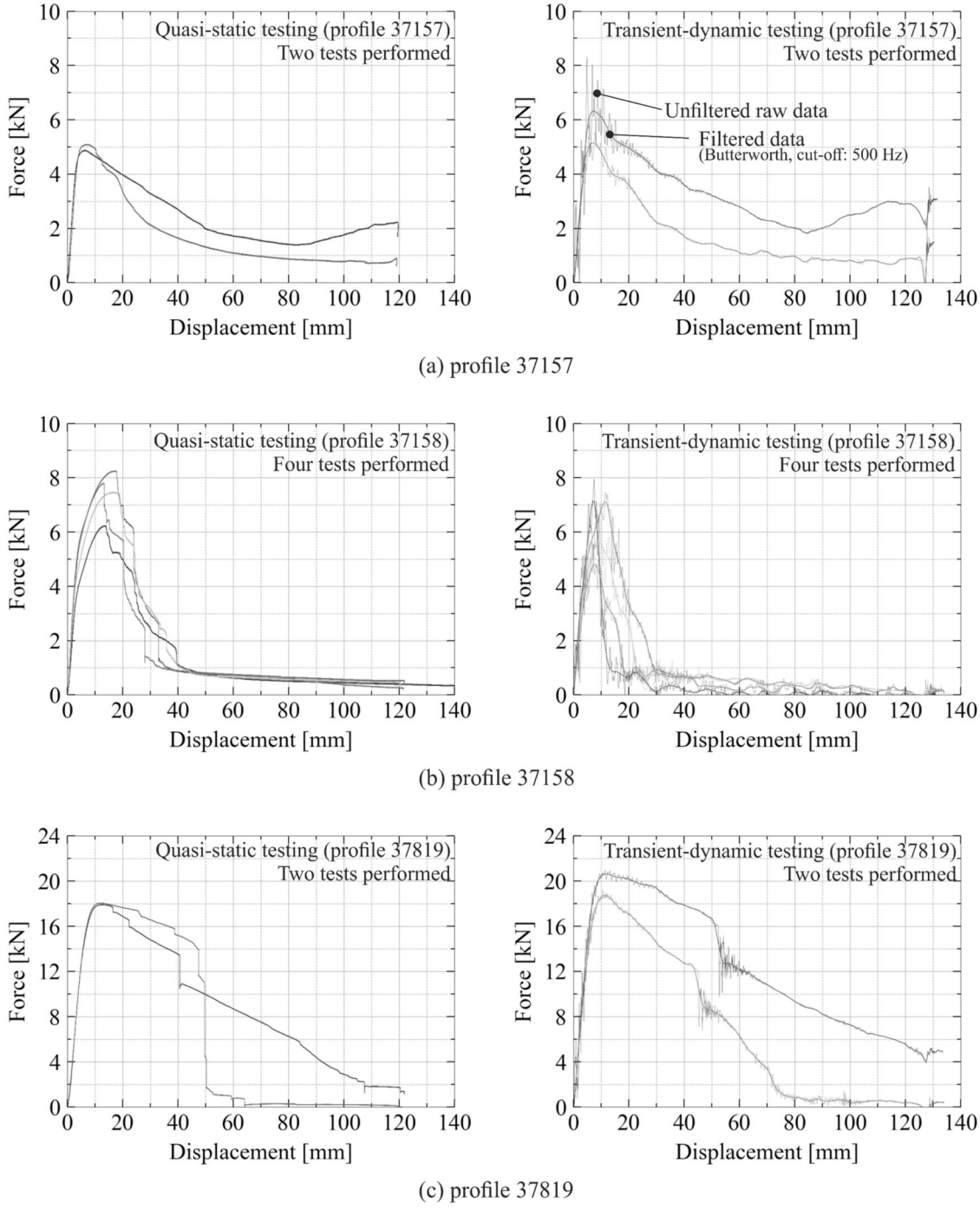

Figure 5. Results of element level test campaign for profiles 37157, 37158, 37819; plots of force-displacement measurements of quasi-static tests (left) vs. transient-dynamic tests (right).

a clamping insert, which was used in the test setup to mount the test specimen on the fixation plate. At this state, contact with the clamping insert led to increased compression loading and buckling of the gusset. Hence, the onset of gusset buckling is driven by the test setup specific insert which consequently needs to be considered in the simulation.

3.2.2. Base corner testing

As illustrated in Figure 9(a), two different base corner types were extracted from the containers, which are base corners AIB (aft-inside-base) and FIB (forward-inside-base). Corner AIB consists of sheets at both sides and a 'filigree' stanchion design, while corner FIB, extracted from the door side, has only one side equipped with a sheet but provides a reinforced vertical profile section of increased wall thickness (stanchion of 'massive' design).

Quasi-static and transient-dynamic testing was performed. For the quasi-static testing a Zwick 1494 electromechanical universal 500 kN testing machine was used while the dynamic tests were performed in a drop tower. The test setups are shown in Figure 9(c1,c2). For quasi-static testing, the base corner specimens were clamped on the T-slots of

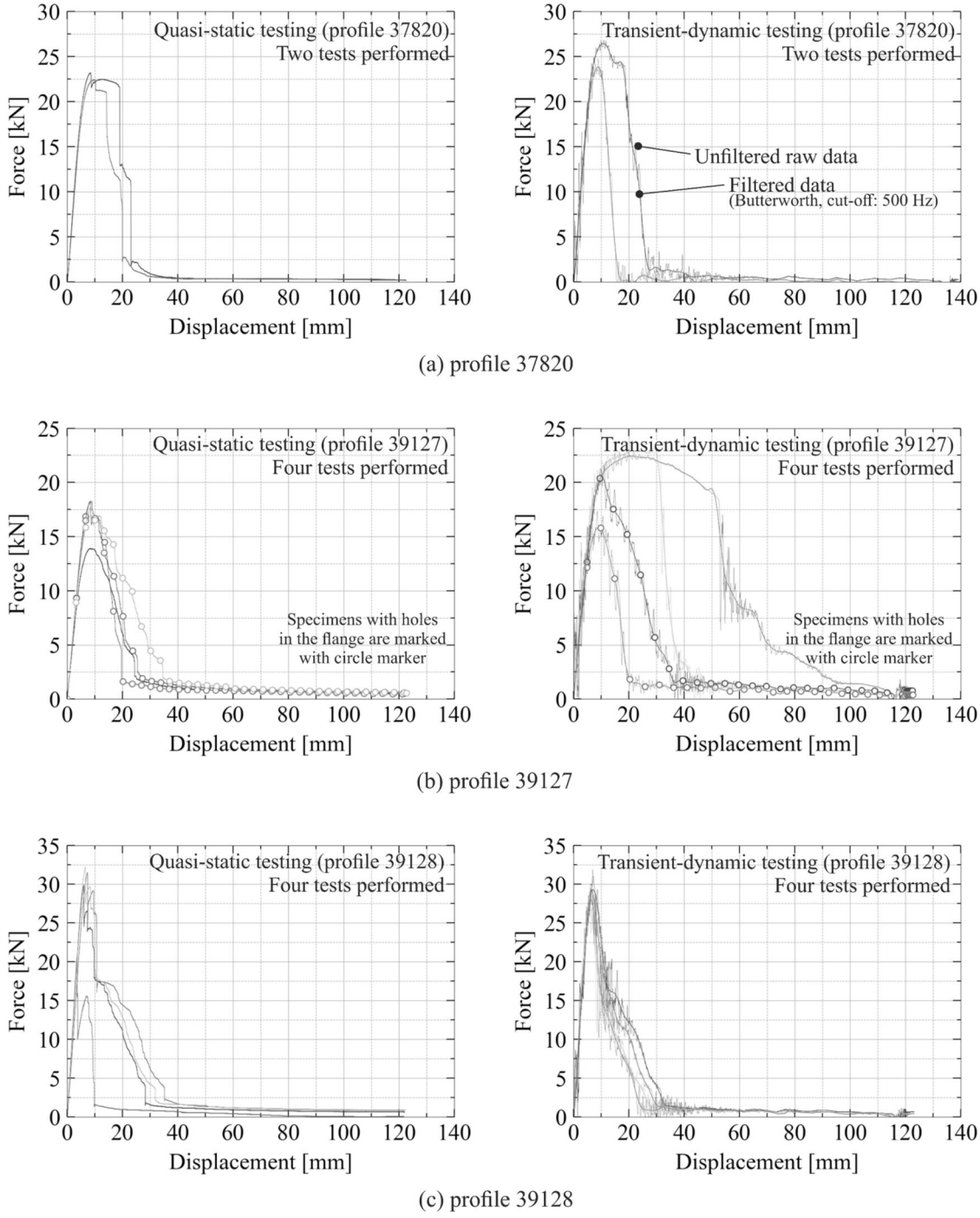

Figure 6. Results of element level test campaign for profiles 37820, 39127, 39128; plots of force-displacement measurements of quasi-static tests (left) vs. transient-dynamic tests (right).

the test machine and loaded in compression by the test machine loading stamp. The quasi-static nominal loading rate was 50 mm/min. The strain gauge load cell of the test machine was used for force measurement at the loading stamp. For dynamic testing, the base corner specimens were clamped on a dynamometer which consisted of three piezo-electrical load cells of type Kistler 9081B. The dynamic crush forces were introduced by the drop tower sled with a nominal loading rate of 4 m/s. The drop mass was 253.0 kg for AIB corner tests and 327.5 kg for FIB corner tests. The force results presented in this article were measured with a sampling rate of 100 Hz for quasi-static testing and 100,000 Hz for dynamic testing. Force signals were synchronised with the high-speed video camera. For both test setups, one high-speed camera of type FASTCAM SA-Z recorded the test sequences in a front view position with frame rates of 50 fps for quasi-static testing as well as 25,000 fps for dynamic testing. The displacements were measured by Digital Image Correlation (DIC) using the high-speed video records and the GOM Correlate software.

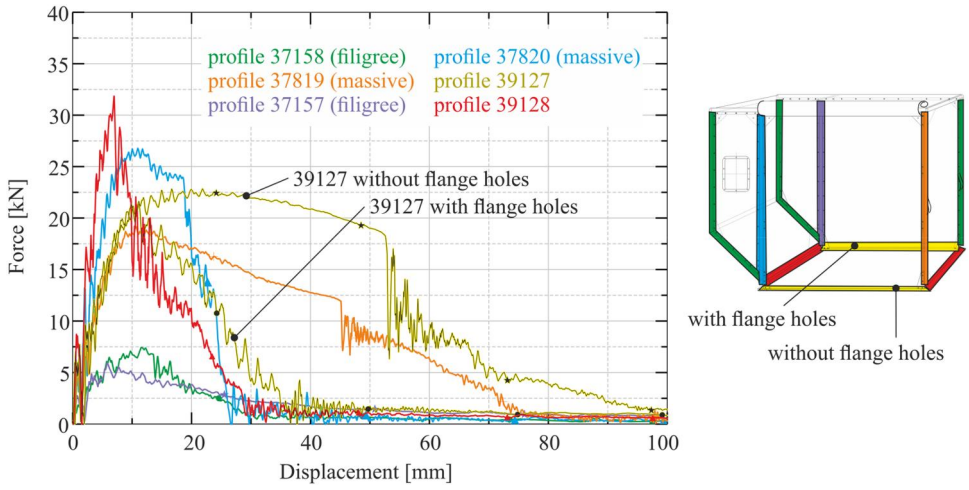

Figure 7. Selected results of element level test campaign showing the range of force-displacement response, one test per profile section type is shown.

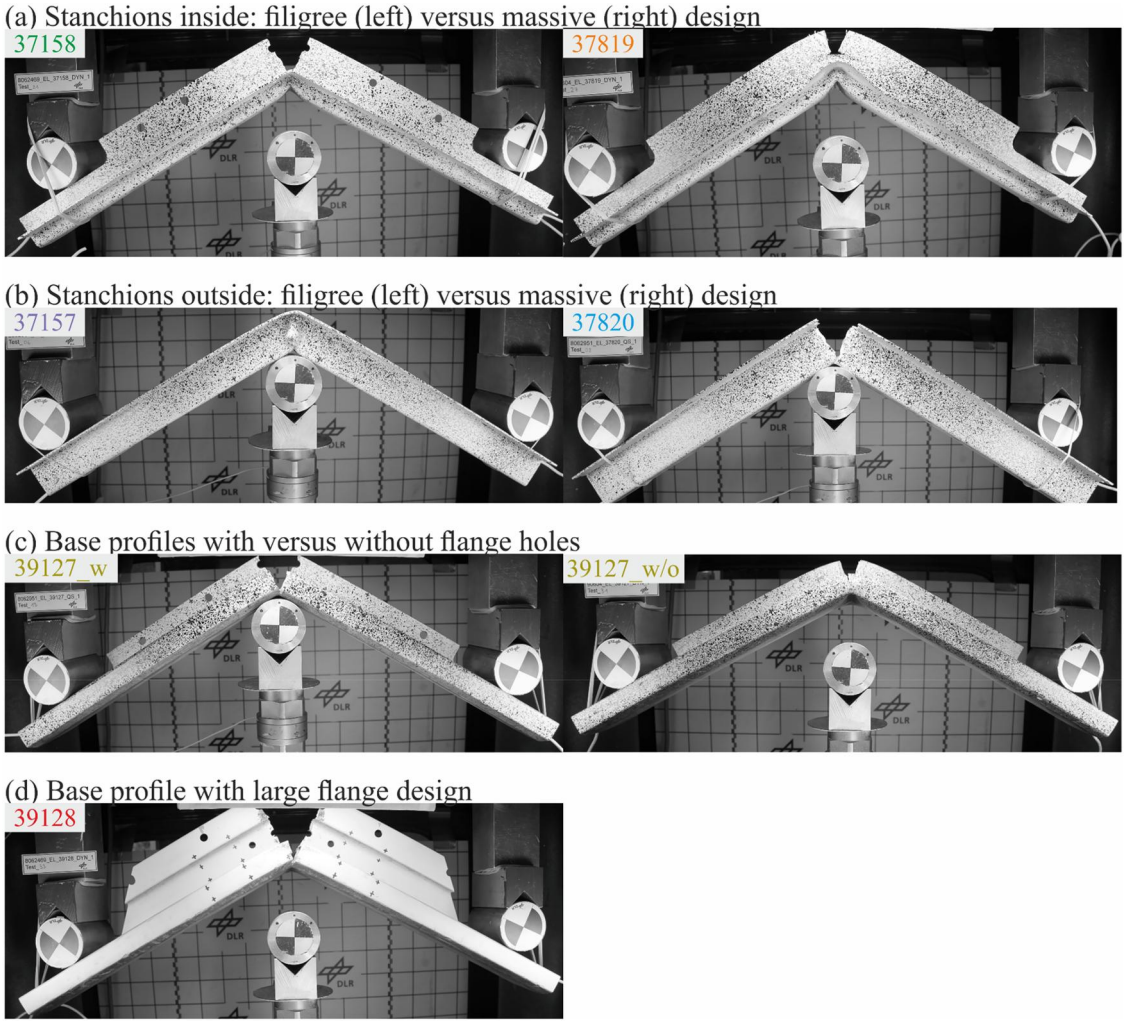

Figure 8. Profile section failure behaviour dependent on profile design.

Force signals of the dynamic tests were filtered with a Butterworth filter and a cut-off frequency of 500 Hz, all other results are unfiltered.

Results of all base corner tests, in terms of force-displacement measurements, are presented in Figures 14 and 15. Representative failure effects based on exemplary tests are shown in Figures 16 and 17.

Non-linearities in the force-displacement curves prior to reaching the maximum force are caused by clearances in the bolted joints as well as deformation of the base profile cross section and sheet buckling. The peak force is driven by complex structural interactions: Compliance in the base corner structure, in terms of bolted joint clearance, and deformation of the base profile cross section and sheet

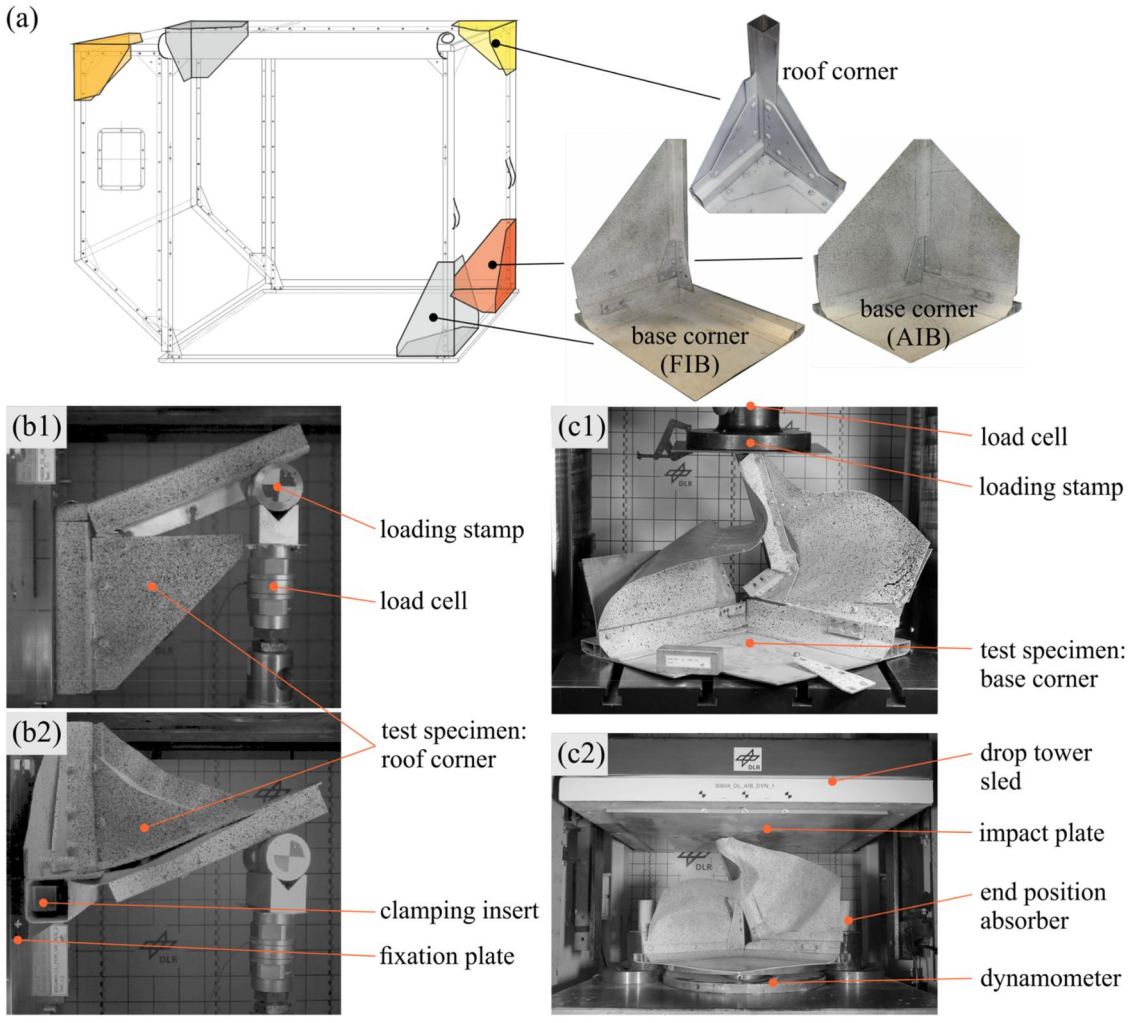

Figure 9. Detail level test campaign, (a) tested corner assemblies, (b) roof corner test setups with (b1) tension mode and (b2) compression mode, (c) base corner test setups for (c1) quasi-static testing and (c2) dynamic testing.

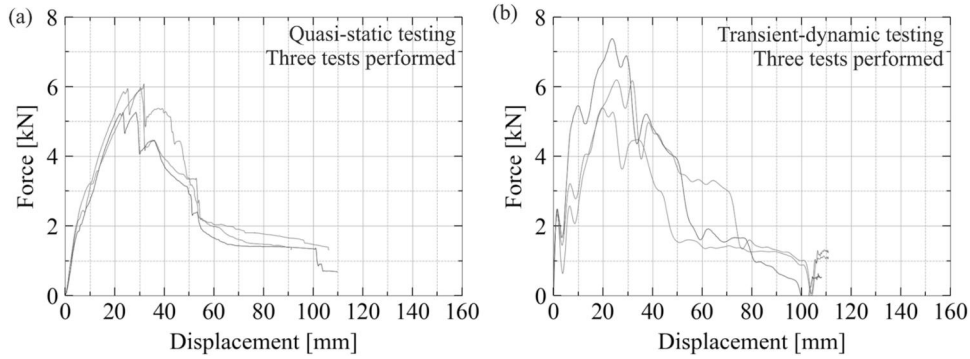

Figure 10. Results of detail level test campaign, plots of force-displacement measurements of all roof corner tension mode bending tests, (a) quasi-static tests, (b) transient-dynamic tests.

buckling led to contact interaction between the vertical stanchion and the base profile sections prior to bolted joints failure. Hence, peak force at the end of the elastic regime is the sum of maximum forces simultaneously transmitted through the bolted joints and through the contact interaction between vertical stanchion and base profile sections.

Main failure in the post-peak regime is attributed to the vertical stanchion as well as the bolted joints. Both main failure effects led to a partly disintegration of the vertical stanchion from the container base structure, enabling the stanchion to globally buckle. After disintegration from one gusset the respective other gusset remains attached and bends together with the attached stanchion. The AIB base corner with its filigree vertical stanchion design showed stanchion buckling directly above the gusset that provided lateral support until disintegration of the assembly initiated.

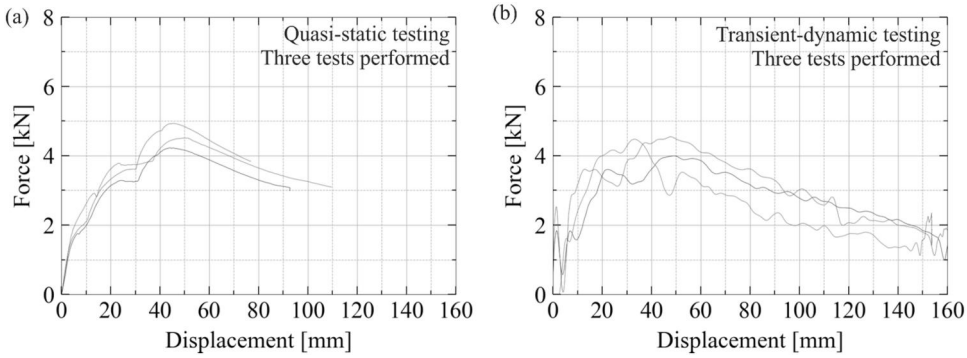

Figure 11. Results of detail level test campaign, plots of force-displacement measurements of all roof corner compression mode bending tests, (a) quasi-static tests, (b) transient-dynamic tests.

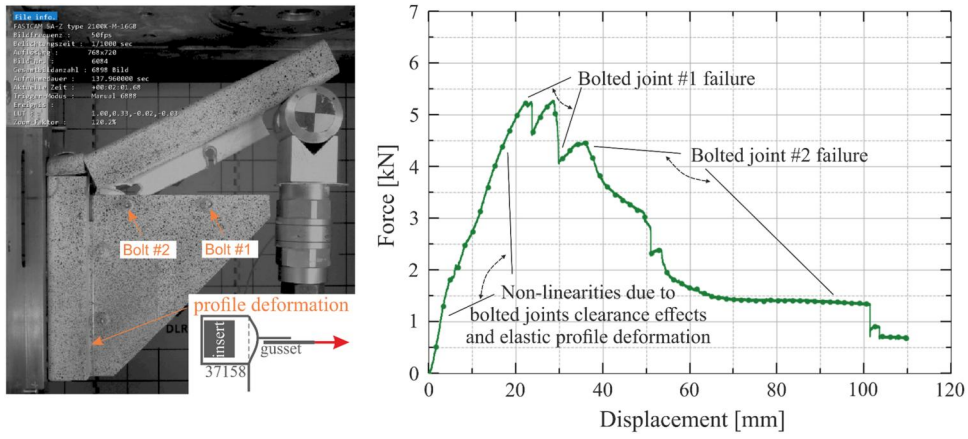

Figure 12. Representative failure effects of roof corner tension mode bending tests, exemplary test curve.

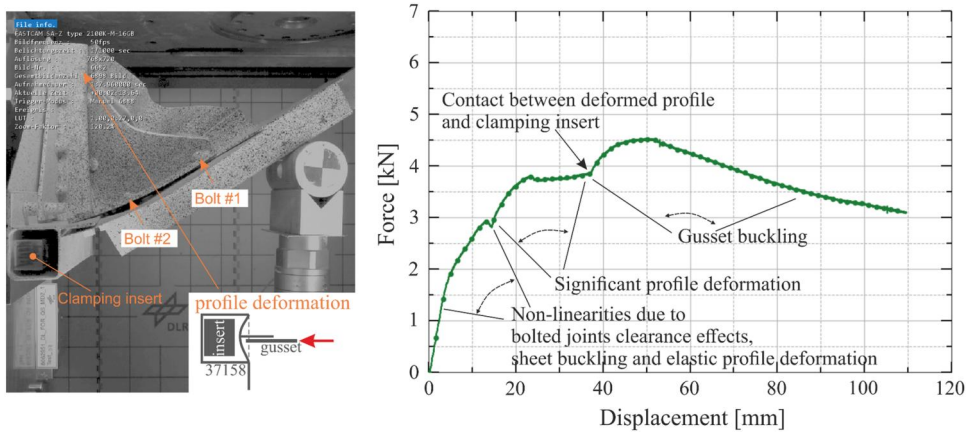

Figure 13. Representative failure effects of roof corner compression mode bending tests, exemplary test curve.

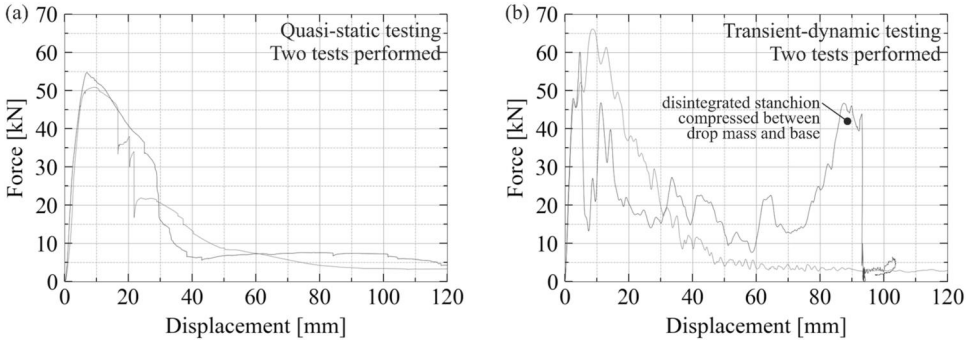

Figure 14. Results of detail level test campaign, plots of force-displacement measurements of all AIB base corner crush tests, (a) quasi-static tests, (b) transient-dynamic tests.

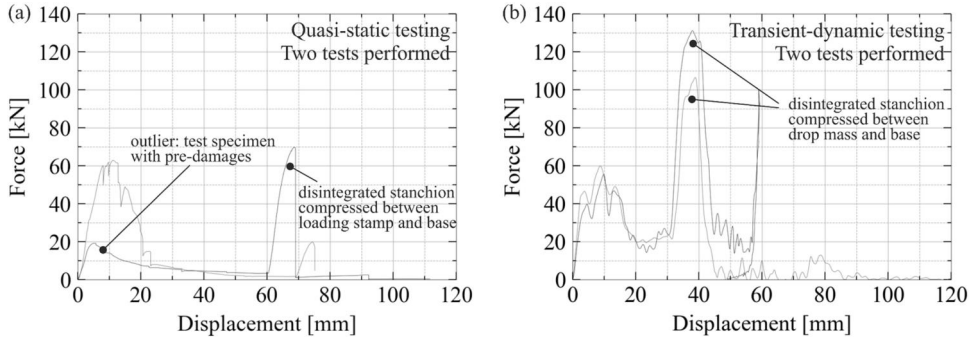

Figure 15. Results of detail level test campaign, plots of force-displacement measurements of all FIB base corner crush tests, (a) quasi-static tests, (b) transient-dynamic tests.

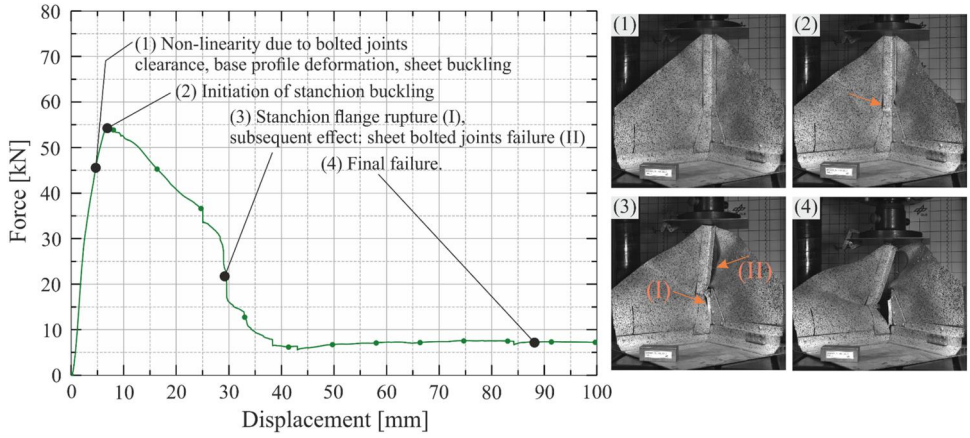

Figure 16. Representative failure effects of AIB base corner crush tests (filigree stanchion design), exemplary test curve.

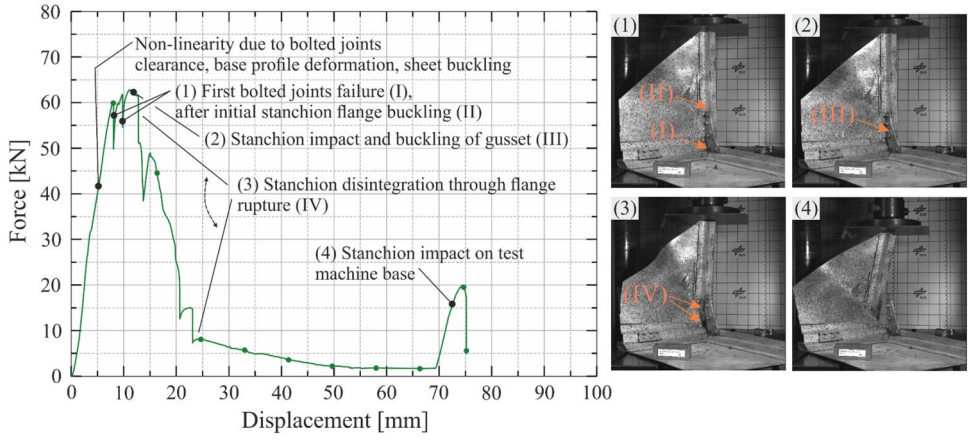

Figure 17. Representative failure effects of FIB base corner crush tests (massive stanchion design), exemplary test curve.

This can be seen in Figure 16. In contrast, this buckling effect was not observed for the FIB base corner with its massive stanchion design. However, the reinforced stanchion of the FIB corner showed no effect on the peak force as other effects such as disintegration of the assembly and parallel load path interactions are dominant in influencing the peak load. Hence, comparing the force-displacement measurements of AIB and FIB base corners for quasi-static testing, similar peak forces and general force-displacement characteristics were observed, as can be seen in an exemplary direct comparison in Figure 18. For dynamic testing, different post-peak regimes of AIB versus FIB base corners were observed, as after disintegration the massive stanchions of the FIB base corners were compressed between base profile and drop mass leading to a high force spike.

3.3. Full-scale level testing

At the full-scale level, the containers were tested under vertical crushing, which is a loading condition that is expected in the cargo hold during an aeroplane crash.

It was decided to test variations of door canvas and door diagonal ropes to identify their influence on the container crash behaviour, and based on that test results to draw

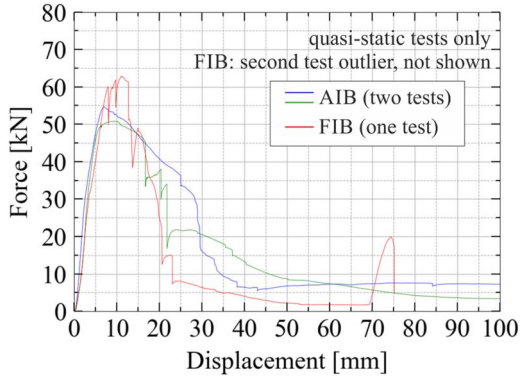

Figure 18. Comparison of AIB versus FIB base corner, force-displacement curves of quasi-static testing.

conclusions on the need of considering door canvas and ropes in the finite element models. Variations with luggage were not considered to experimentally determine the failure behaviour of the container structure itself, hence all tests were performed with empty containers. It is expected that separately validated luggage models, based on literature data [4,5], and container models can subsequently be combined in numerical simulation applications. With that approach, the test matrix for the eight full-scale tests allowed for one repeat test per variant and considered the container type as well as door canvas/ropes as parameters. The test matrix is given in Table 1. A nominal impact speed of 6.7 m/s (22 ft/s) was selected.

As the tested containers were used containers taken from the fleet, a thorough inspection of each container was performed and all damages were mapped in detail prior to testing. After each test, all post-test failures were inspected and mapped to identify potential correlation between pre-test damages and failure effects during the test. In all tests, there was only one failure effect during a crash test for which the location of stanchion plastic hinge correlated with a pre-test damage repair. Based on that outcome the experimental results can be seen as independent of pre-damage and wear effects.

For the temporary vertical drop test setup, a proper base was required, capable to sustain the dynamic impact loads. The selected ambos concept made use of the massive span field at the Institute's test lab which provides an effective ambos mass of 79 tons.

Different test setup configurations were considered and assessed with the aim to provide proper boundary conditions for test measurements as well as for the finite element simulation. The final test setup is shown in Figure 19. The container is positioned on a test base and a free-falling unguided impact plate crushes the container. With the container positioned on a test base, favourable test conditions are given to enable force measurements at the four base corners directly below the vertical stanchions of the container. The free-falling and unguided impact plate may end up in rotations during container crushing in case of asymmetric container collapse, but the free boundary conditions of the impact plate can precisely be reproduced in the finite element simulation. In addition, it was expected that the rotations of the impact plate remain small due to the plate inertia, at least during the relevant part of the test.

The test setup made use of the identical base dimensions of the AKE and AKH containers so that one test base could be used for all tests. The container is embedded on four piezo-electrical load cells of type Kistler 9081 A, enabling force measurement at each base corner. The impact plate had a mass of $m = 882.0$ kg, dimensions of 3000 mm × 2000 mm, and was designed for maximum rigidity. Elastic ropes were installed that automatically aligned the impact plate with the container while lifting the plate to the desired drop height. A pyrotechnical system was used to release the impact plate. End position absorbers were installed to stop the impact plate in case of a brittle container collapse with minor energy absorption.

Data acquisition comprised the vertical forces measured separately at each base corner and four high-speed cameras of type FASTCAM SA-Z. Two cameras were positioned at the front respectively rear side of the container, and two cameras were positioned with an isometric view on the container front and rear side. In addition, two GoPro Hero 10 cameras were installed at different positions for some tests. The force signals were recorded with a sampling frequency of 50,000 Hz using a NI-DAQ transient recorder that was synchronised with the high-speed cameras. The cameras recorded with a frame rate of 5000 fps. The displacements were measured by Digital Image Correlation (DIC) using the front and rear high-speed video records and the LIMtrack software. Force signals were filtered with a Butterworth filter and a cut-off frequency of 1000 Hz, all other results are unfiltered.

Results of all full-scale container tests, in terms of force-displacement measurements, are presented in Figures 20 and 21. The total force as the sum of the four load cell forces is presented. The displacement corresponds to the mean displacements of four DIC measurements at the front and rear side of the impact plate. The results show good repeatability with an overall correlation according to ISO 18571:2014 ranging between fair and good [13]. This is an important result as, for the tested containers, potential stochastic effects of detailed failure modes, partly seen at element and detail level, do not result in a large mean variation at full-scale level. Representative failure sequences for both container types are illustrated in Figures 22 and 23, showing exemplary tests.

From the force measurements and high-speed video records, identical general crash phases can be identified for both container types. After first impact, the roof and base corners, respectively the stanchion upper and lower attachments, are crushed leading to a first characteristic force peak. Details from high-speed video records in Figure 24 show this corner crushing which reveal the same effects as identified in the base corner crush tests at the detail level. After container corner disintegration, the stanchions hit the base profiles and subsequently are highly compressed between impact plate and base profile leading to a second characteristic force peak and stanchion buckling respectively formation of a stanchion plastic hinge. This second

Table 1. Test matrix for full-scale level testing (FSL: full-scale level, DYN: dynamic test).

Test number	Container type	Door canvas and diagonal ropes	Test identifier (incl. series number)
1	AKE	With	8062447_FSL_AKE_DYN_1
2	AKE	With	8062445_FSL_AKE_DYN_2
3	AKE	Without	8063050_FSL_AKE_DYN_3
4	AKE	Without	8062915_FSL_AKE_DYN_4
5	AKH	With	8063189_FSL_AKH_DYN_5
6	AKH	With	7059356_FSL_AKH_DYN_6
7	AKH	Without	7059334_FSL_AKH_DYN_7
8	AKH	Without	8063217_FSL_AKH_DYN_8

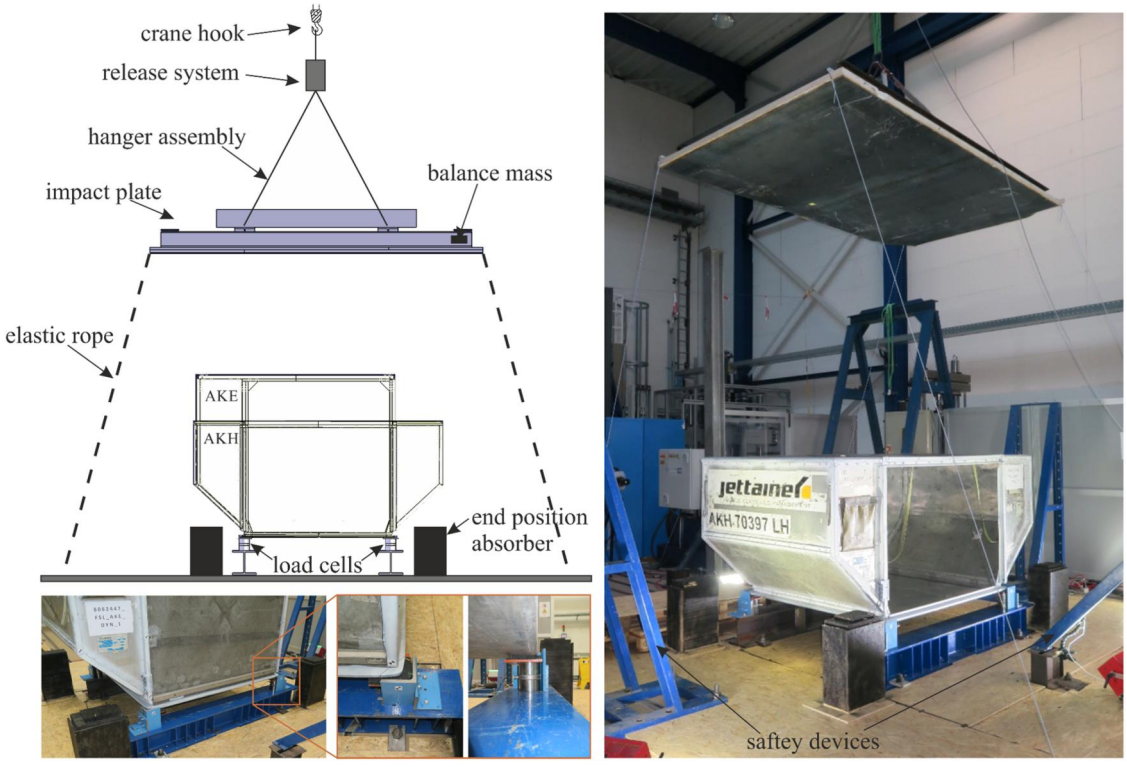

Figure 19. Full-scale test setup.

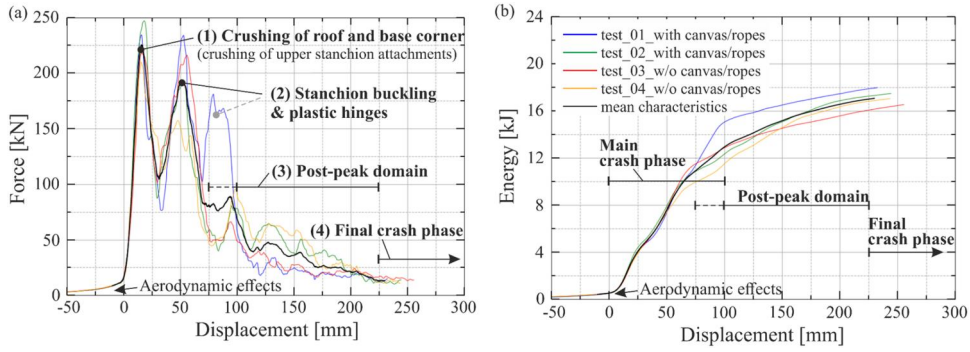

Figure 20. Results of full-scale level test campaign for all tested AKE containers, (a) plots of force-displacement measurements, (b) energy-displacement curves.

characteristic force peak was less distinct for the AKH containers as the rear stanchion upper attachments completely disintegrated during the first peak leading to stanchion rotation instead of buckling, as can be seen in Figure 23. For the AKH container, the upper attachment of the rear stanchions is not a corner assembly but a plane assembly, hence less stability is provided by the container structure which led to more distinct disintegration of the stanchions and a less distinct second characteristic force peak compared to the AKE containers.

In the subsequent post-peak domain for a total displacement beyond $d = 75$ mm, the container failure kinematics are fully developed and the force-displacement characteristics are dominated by further development of stanchion plastic hinges respectively stanchion failure. Further secondary effects of the post-peak domain are failures of the

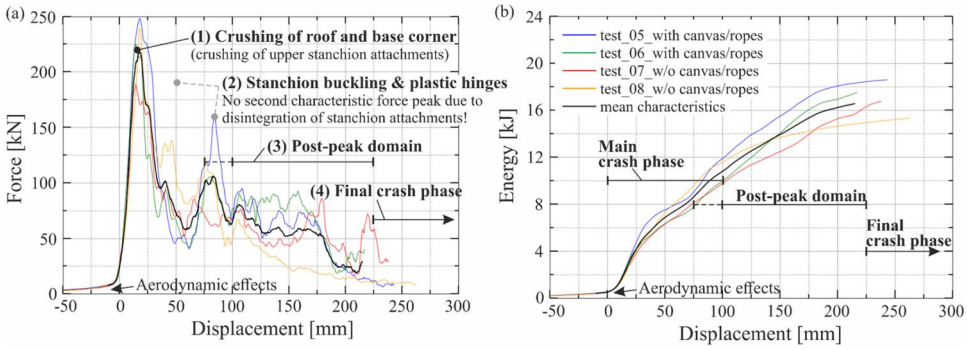

Figure 21. Results of full-scale level test campaign for all tested AKH containers, (a) plots of force-displacement measurements, (b) energy-displacement curves.

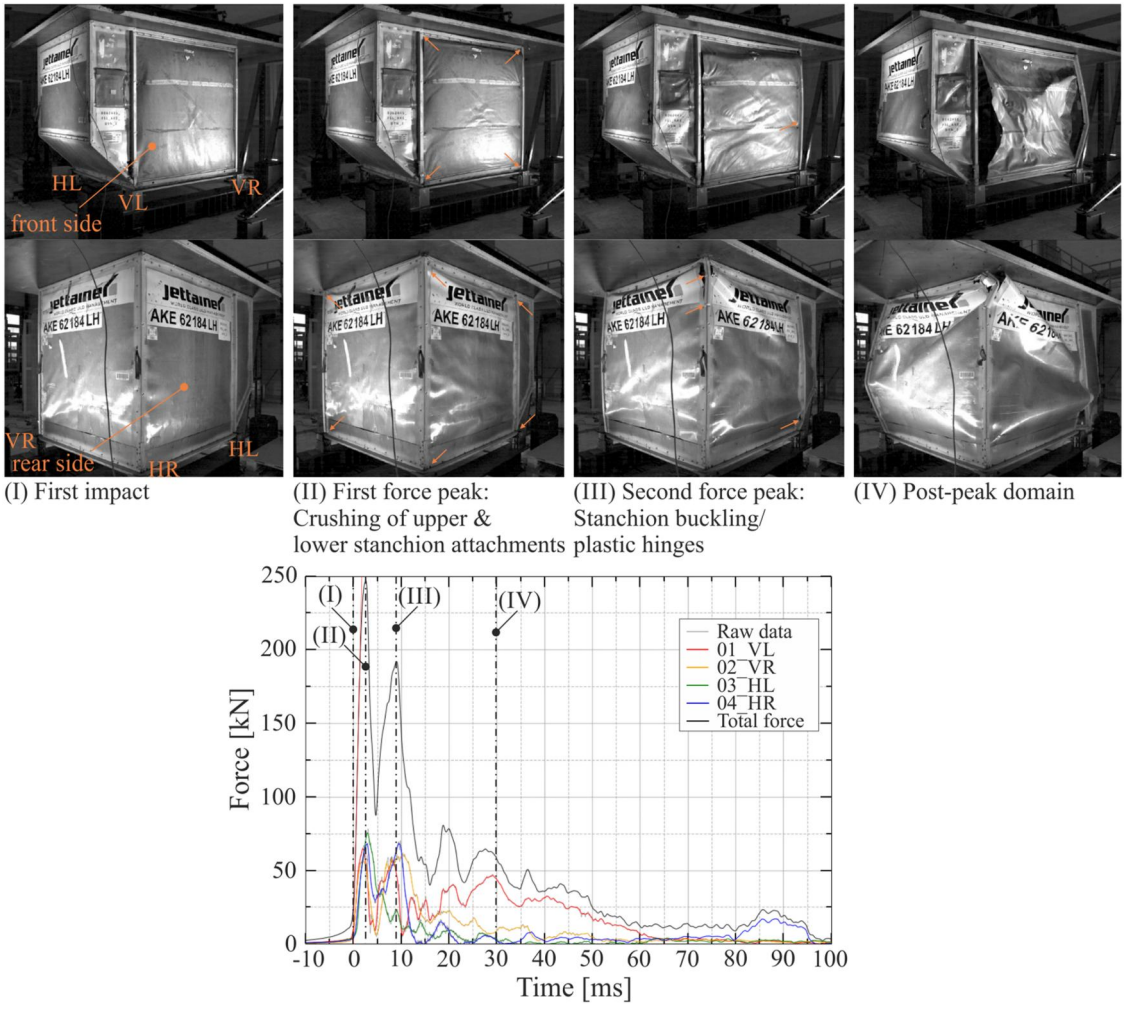

Figure 22. Failure sequence of AKE container, exemplary test with door canvas and ropes.

container balcony structure with plastic deformation or rupture of the 45 degrees corner assemblies, partly further plastic hinges in the balcony profile sections, and sheet detachment due to bolt pull-through or shear-out failure. At a total displacement of approx. 225 mm, the post-peak domain reaches asymptotic low force values which indicates the final crash phase.

Note that the force-displacement curves show non-zero force values prior to contact between impact plate and container, at displacement $d = 0$ mm. This circumstance can be attributed to aerodynamic effects. The free-falling flat impact plate of dimensions 3000 mm × 2000 mm has an aerodynamic drag and creates an air cushion between impact plate and container roof. The load cells at the container base measured these loads from the air cushion with total forces of approx. 10 kN prior to contact. This is a significant pre-loading with favourable effects as the container is pressed against the load cells prior to impact which prevents potential contact ringing. Note that the air cushion force does not affect the peak force measured in the test, and is not related to additional energy added to the system.

With regard to the test matrix parameter 'container type' identical general crash phases for both container types were identified. The initial peak forces are in the same range,

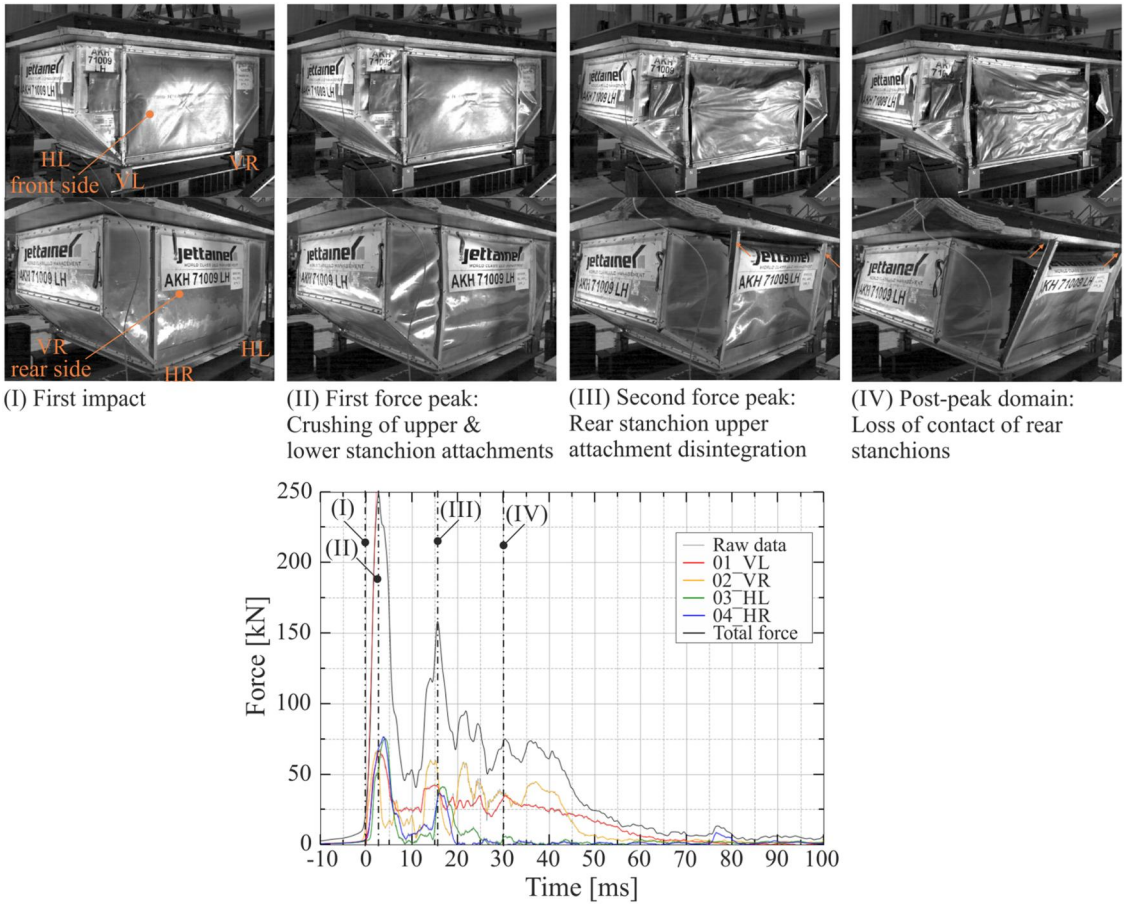

Figure 23. Failure sequence of AKH container, exemplary test with door canvas and ropes.

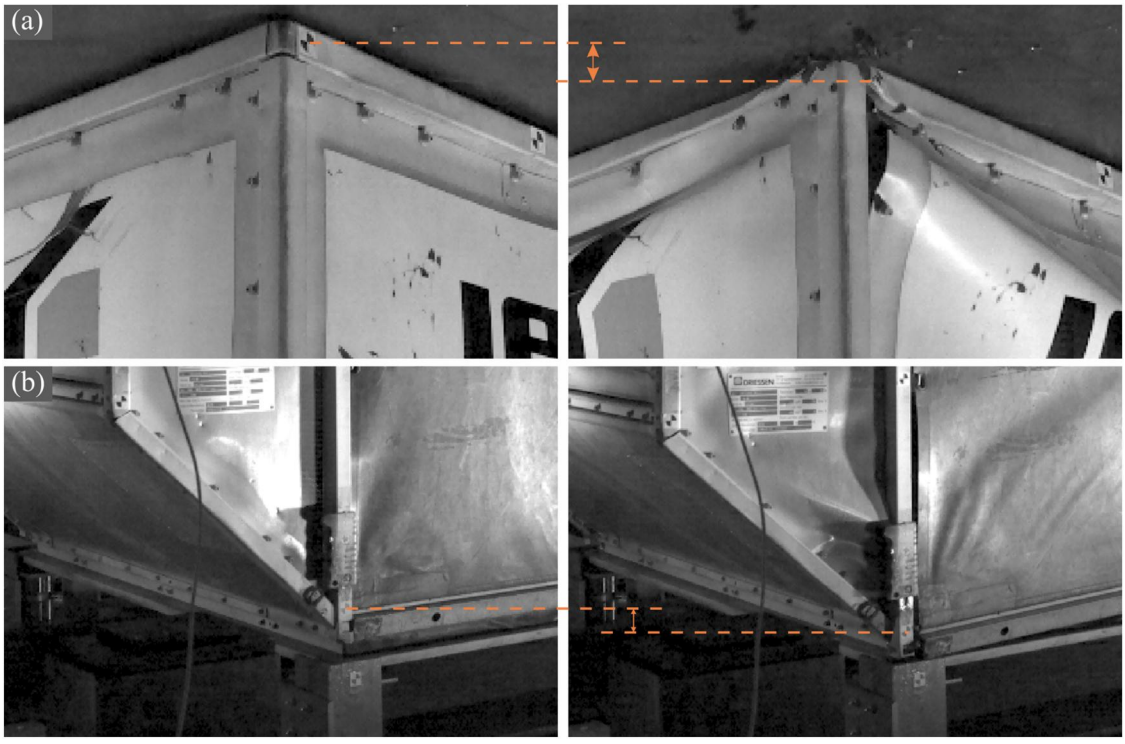

Figure 24. Crushing of upper and lower stanchion attachments during the first characteristic force peak, (a) roof corner HR, (b) base corner VL, exemplary test.

which is a reasonable result due to the design similarities of both container types and the fact that the first characteristic force peak is not driven by the stanchion length but by the crushing of the stanchion attachments. The second characteristic force peak is different regarding AKE versus AKH containers due to different stanchion upper attachment and hence different extend of stanchion disintegration. The post-peak domain is different regarding AKE versus AKH containers due to the stanchion length that influences the load level for plastic hinge developments as well as due to the number of balconies that are crushed. Altogether, the total absorbed energies are in the same range for both container types.

With regard to the test matrix parameter 'door canvas and ropes' the test results indicated no noticeable influence of door canvas and diagonal ropes. The force-displacement results were in the same range and no effect could be identified by high-speed video records or post-test inspections that shows any influence of door canvas and diagonal ropes. This outcome indicates that door canvas and diagonal ropes may not need to be considered in finite element models as they do not contribute to stanchion stability.

4. Finite element simulation

In this section, selected outcomes from the development of container simulation models are presented. A shell-element modelling was selected for all container parts and connector elements were selected for modelling the bolted joints. All simulations were performed using the explicit finite element software Abaqus/Explicit, versions 2016 through 2020. Conventional shells of reduced integration (S4R) were used. Load introductions such as loading stamps were modelled using analytical rigid surfaces, the impact plate was modelled as rigid body. A friction coefficient of $\mu = 0.2$ was applied.

As discussed in section 2, material characterisation at the coupon level was not performed in the scope of this study as data sheet information provided by the container manufacturer was considered as sufficient.

4.1. Element level simulation

The profile sections tested at the element level provided different levels of complexity and were used to stepwise calibrate and validate the finite element models.

Profile sections without any drill holes (profile 37819) or with in-plane holes that did not serve as crack initiator (profile 37157) were used to calibrate the material input data against the three-point bending test results. Profile sections with out-of-plane holes that served as crack initiators (profile 39128) were used to calibrate the Discretisation and meshing of the bolted joint holes. Finally, the more complex profiles section with out-of-plane holes of different hole patterns (profile 37158) and combination of sections with and without holes (profile 39127) were used to validate the selected modelling approach for the profile sections.

For the aluminium alloys of 7000 series a simple bi-linear stress-strain law was assumed with isotropic hardening based on the Mises yield surface (*plastic, hardening = isotropic). Material input data were taken from manufacturer data sheets, except the linear hardening curve and failure strain which were selected as calibrating parameters at the element level. Strain rate dependency was not applied in the material model as the profile section material is aluminium which generally show low strain-rate effect [14,15]. Strain-rate effects visible in the experimental tests at element and detail level can be attributed to structural effects such as strain-rate dependent buckling strength. The structural strain-rate effects are captured by the finite element modelling.

A target element size of 10 mm was selected for the full-scale container model, based on expected and acceptable calculation times, and also applied for the element level simulations. Smaller element sizes were additionally considered to check for element size dependencies. In the experiments, it turned out that three-point bending for profile sections with more filigree design led to bending stamp indentation effects with local plasticising effects. In the simulations, element sizes in the range of 4 mm were necessary to capture these effects, which are test-specific and not representative for stanchion buckling and plastic hinge formation. In contrast, profile sections with stiffer design showed no local indentation and the finite element simulations captured well the experimental results with a nominal element size of 10 mm.

The simulations showed minor influence of the bolt holes on the maximum force but significant influence on the force drop after failure initiation. This effect was also observed in the experiments, as exemplarily shown in Figure 7 for profile 39127 which shows only approximately 5% higher maximum force for tests without bolted joint holes compared to drilled sections while the force drop significantly differs for both variants of profile 39127. The corresponding simulations of profile 39127 are presented in Figure 25 and exemplarily show the simulation capability to sufficiently accurate represent the force-displacement response dependent on the presence or absence of drill holes in the section flange.

The dominant failure mode of the container under crush loading was expected to be stanchion buckling. Considering the minor influence of bolt holes on the profile section bending strength it can be concluded that neglecting the bolt holes in the model Discretisation may be a reasonable approach that still was expected to be capable to capture the main failure effects of the container. With that conclusion, outcomes of the element level simulation were (a) the confirmation of an element size of 10 mm, (b) the confirmation of a modelling approach without bolted joint holes, and (c) the material input data calibrated with a Yield stress of 0.3 GPa and a failure strain of 0.23 for the nominal element size of 10 mm.

4.2. Detail level simulation

The container corner structures, tested at the detail level under different loading conditions, were used to validate the bolted joints modelling and the model assembly.

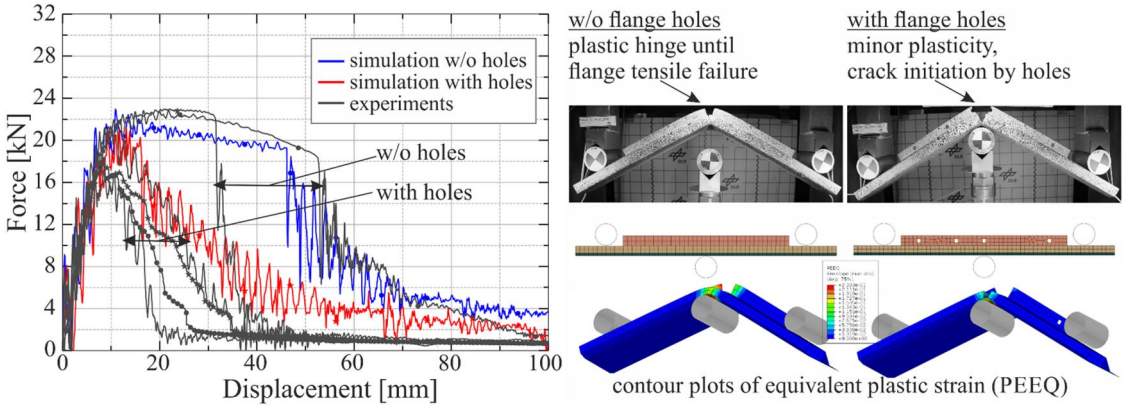

Figure 25. Element level simulation with calibrated material input data for profile 39127 variations with versus without bolted joint holes in the flange.

Connector elements were selected for modelling the bolted joints using the mesh-independent fastener option in Abaqus/Explicit (*fastener). Connector modelling aligned with the approach presented in [16]. Connector stiffness was separately defined for the six components (*connector elasticity, component). Connector plasticity described combined yielding in tension and shear direction (*connector potential). Connector hardening was described based on the equivalent plastic relative motion (CUPEQC). For connector damage initiation, the plastic motion criterion was selected (*connector damage initiation, criterion = plastic motion) and connector damage evolution was defined with linear softening based on type motion (*connector damage evolution, type = motion).

Connector input data were taken from manufacturer data sheets and supplemented with analytical determination as well as assumptions. The general connector input data is a simplified tri-linear force-displacement characteristic as shown in Figure 26 and was adapted for each bolted joint according to the analytically determined bearing strength as well as tensile strength. In shear direction, failure initiation is assumed at a displacement of 10 mm assuming shear-out failure for the considered bolt hole edge distance. The selection of a simplified tri-linear force-displacement characteristic is based on experimental test data on bolted joints which generally can be described by a tri-linear correlation [17].

Detail level simulations were performed based on the calibrated material input data of the element level. Simulations were performed with nominal element sizes 4 mm and 10 mm, to check for potential mesh dependencies.

4.2.1. Roof corner simulations

The roof corner finite element model is depicted in Figure 27, the fastener models are highlighted. Relevant portions of the test setup are considered in the model which also comprises clamping inserts as well as reinforcement inserts which were installed in the profile sections to enable load introduction without local damage or indentation.

Force-displacement results of finite element simulation versus experiments are presented in Figure 28. The comparison for tension mode bending, Figure 28(a), shows generally fair agreement in particular with regard to bolted joint failures which occur in the same displacement range for simulation versus experiments. The comparison of compression mode bending, Figure 28(b), shows element-size dependencies and generally poor agreement. The simulation with element size of 10 mm provides only four elements over the width of the profile section and hence was not able to capture in detail the profile section deformation introduced by the compression loaded gusset. This is why in Figure 28(b) the simulation result for 10 mm element size shows linear progression up to a displacement of 25 mm while the simulation with 4 mm element size follows the non-linear response of the experiments. However, both element sizes are not capable of simulating the true profile section deformation, see Figure 29, for which reason none of the simulations experienced contact with the clamping insert that led to a characteristic kink in the experimental curves at displacements between 30 and 40 mm und subsequent higher load level due to the direct load path. Hence, the discrepancies in the simulation can be attributed to the specific test setup and are not related to expected loading conditions of the full-scale container.

In Figure 30, contour plots of the finite element simulations are compared with high-speed video records from the experiments. The simulation results underline the observations from the experiments with the tension mode bending primarily leading to bolted joints failure and the compression mode bending primarily leading to compressive buckling.

Summarised, the finite element simulations were capable of representing the main failure effects while discrepancies in the simulations are related to test specific details which are not relevant for the expected container failure behaviour.

4.2.2. Base corner simulations

The base corner simulations can be seen as a final validation of the model assembly. Especially the non-linear effects discussed in paragraph 3.2.2, that lead to parallel load paths which together describe the maximum failure force of the base corner, should be captured by the simulation.

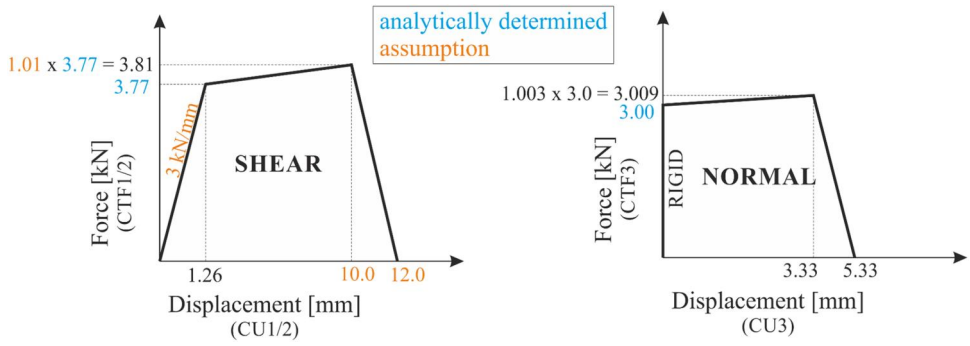

Figure 26. Connector input data defined for the fastener model.

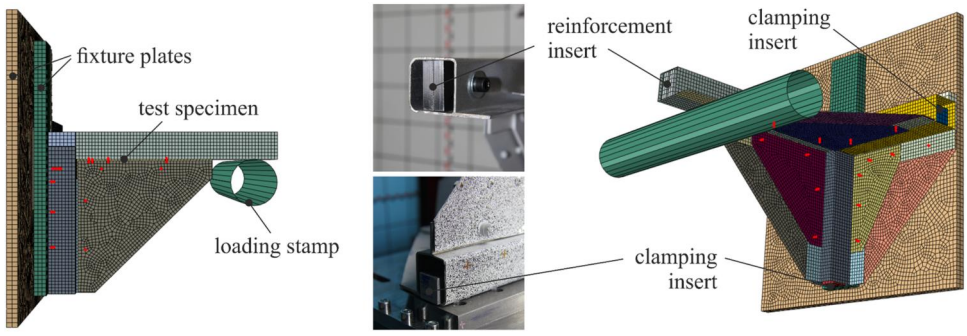

Figure 27. Roof corner finite element model.

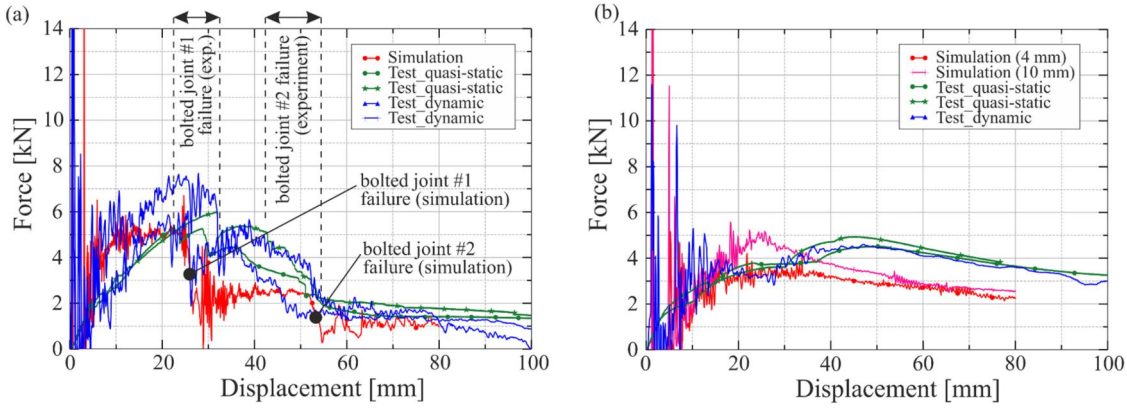

Figure 28. Roof corner force-displacement results of finite element simulation versus experiments, (a) tension mode bending, (b) compression mode bending.

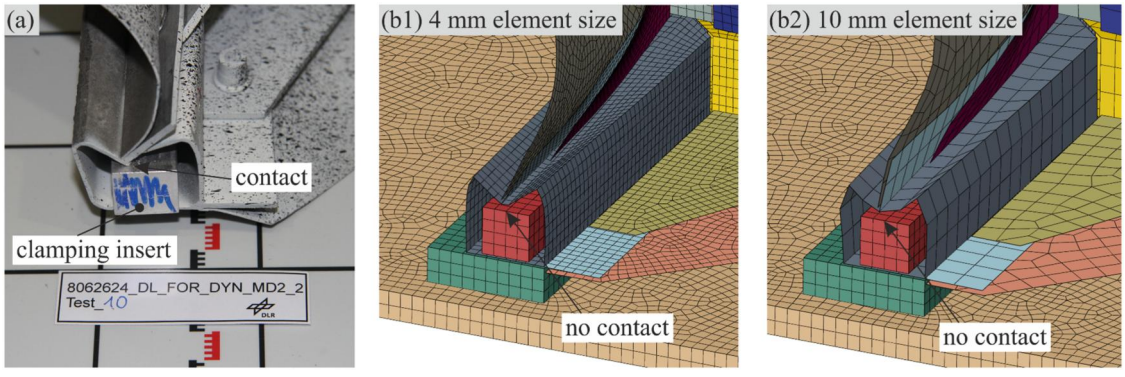

Figure 29. Roof corner compression mode bending leading to deformation of the profile section, (a) experiment showing contact with the clamping insert, (b) simulations with different element size showing no contact.

The presentation of base corner simulations is focused on the AIB base corner, while for the FIB base corner the same modelling was used. The base corner finite element model is depicted in Figure 31, the fastener models are highlighted. The test specific clamping condition is represented in the model. A forging part, the corner piece,

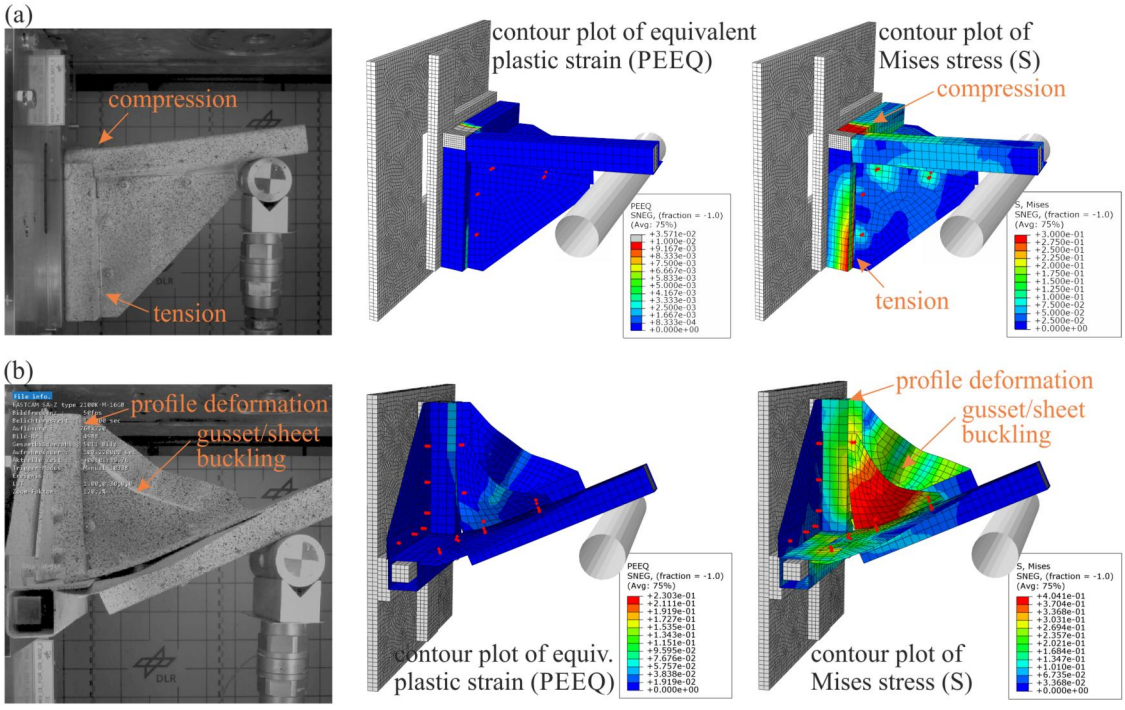

Figure 30. Roof corner finite element simulation versus experiments, (a) tension mode bending, (b) compression mode bending.

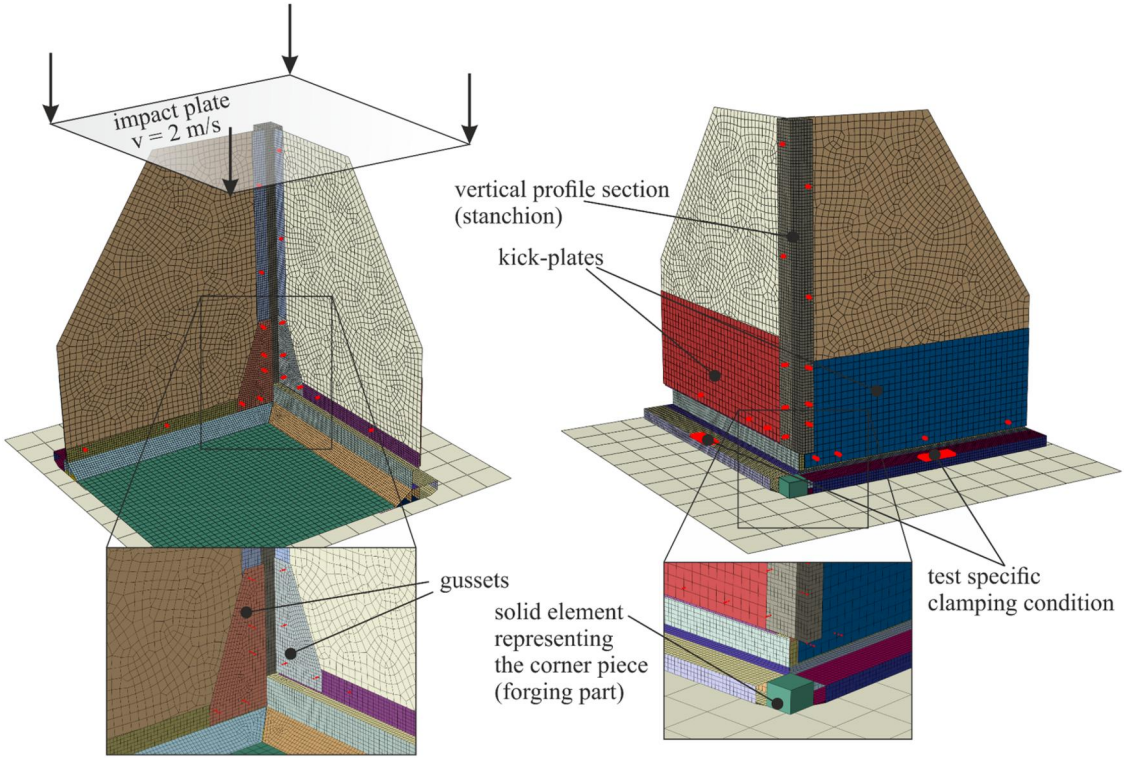

Figure 31. Base corner finite element model, exemplarily shown for AlB base corner.

connects the base profiles of the container and is modelled using solid elements.

Force-displacement results of finite element simulation versus experiments are presented in Figure 32. The main test phase that describes the structural collapse of the base corner up to a displacement of approx. 30 mm is fairly captured by the simulation in terms of general force-displacement characteristics and maximum force. The corresponding effects obtained in the simulation corresponds to the observations from the experiments: Compliance that leads to first contact interaction of the stanchion with the base profile prior to bolted joint yielding due to clearance effects with a parallel load path that results in a first force spike ($d = 4$ mm), fastener yielding and stanchion crushing on the base profile with a second force spike ($d = 13$ mm), and subsequently complete fastener failure and

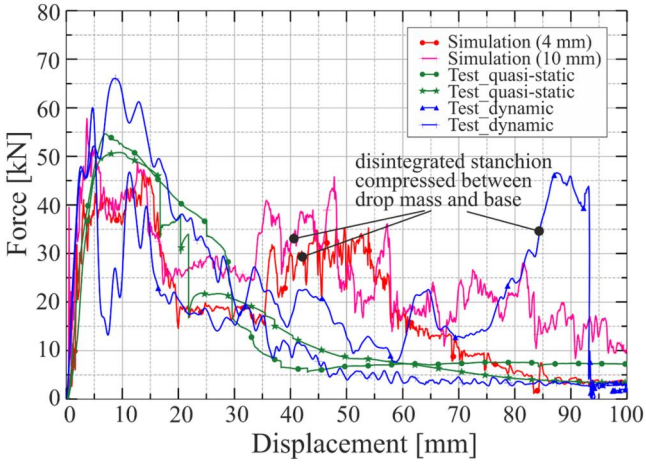

Figure 32. Base corner force-displacement results of finite element simulation versus experiments, exemplarily shown for AIB base corner crushing.

disintegration leading to a force drop in the simulation between $d = 13–18$ mm. Subsequent poor agreement of the simulation with the experiments for displacements larger than 30 mm can be attributed to the progressing failure kinematics of the base corner with the simulation showing the stanchion compressed between drop mass and base. This test specific effect occurred more randomly, and similar behaviour could partly also be observed in the dynamic base corner tests, see Figure 32.

Final failure of simulation versus experiments is exemplarily shown for the AIB corner in Figure 33. The failure kinematics could be well captured by the simulation.

4.3. Full-scale level simulation

Full-scale level simulations were performed based on the outcomes of the element and detail levels. According to the outcomes of full-scale testing, see paragraph 3.3, the container finite element models were built up without modelling the door canvas and diagonal ropes. The nominal element size was 10 mm for the profile sections and gussets, and 20 mm for the sheets. The simulation models for both container types are shown in Figure 34.

Simulation results based on total force and impact plate mean displacement are presented in Figure 35 (AKE container) and Figure 36 (AKH container), and compared with the experimental results. Generally good agreement can be seen for the AKE container simulation, with an underprediction of the initial force spike relative to the experimental mean characteristics of all four tests but still very close to the range of the individual test results, Figure 35(a). The absorbed energy versus displacement is captured well by the simulation, Figure 35(b). The AKH container simulation shows similar good agreement with the experiments except the post-peak domain. The force-displacement response in Figure 36(a) shows an overprediction of the initial force spike relative to the experimental mean characteristics of all four tests but still inside the range of the individual test results. Regarding the post-peak domain generally higher forces are obtained compared to the experiments. The discrepancies in the post-peak domain are related to the rear stanchion failure, which showed significant stanchion rotation after disintegration in the experiments, see Figure 39. Although crushing of the stanchion upper attachment was captured well in the simulation, the rear stanchions stayed vertically and did not rotate so that further stanchion crushing resulted in higher force levels for the simulation than obtained in the experiments, with subsequent stanchion buckling in the simulation, see Figure 39. Minor friction effects between stanchion and impact plate may led to this discrepancy.

Note that the aerodynamic effects are not captured in the finite element simulation which is why the total force prior to impact is zero, see Figures 35(a) and 36(a).

The corresponding crash sequences of the simulations are shown in Figure 37. Good correlation between simulation and experiments was obtained for the crash kinematics in terms of stanchion buckling, the formation of plastic hinges, and disintegration of the sheets due to bolted joint shear-out-failure, as exemplarily shown in Figure 38.

Most important, the simulations captured well the detailed failure effects of the stanchions, which are the main contributions to the force-displacement response (Figure 38, Figure 39, and Figure 40). Exemplary results are shown in Figure 40 and compare the stanchion failure effects of simulation versus experiment. The simulated roof and base corner crushing shows the same effects as observed in the experiments. First, the stanchion upper attachment is crushed while the lower attachment at the base corner remains intact. At this state, the bolted joints of the sheet attached to the stanchion already failed to a large portion leading to early sheet disintegration. Subsequently, the stanchion lower attachment is crushed leading to disintegration and stanchion impact on the container base with stanchion compressive loading close to buckling, as indicated in the contour plot of equivalent plastic strain in Figure 40(b), showing plastic strain directly above the lower gusset.

5. Conclusions

The primary intent of this article is the provision of experimentally determined crash characteristics of air cargo containers that can be used in aeroplane crash analyses. The plots of force-displacement and energy-displacement curves presented in Figures 20 and 21 represent the core results with the full-scale container crash test response. These characteristics may be used for any type of container representation, ranging from analytical models up to detailed finite element models. Additional experimental data at the element and detail level provide further information on the container failure effects that may be used for container model development.

Concerning the experimental testing, the element and detail level tests provide a good range of structural response suitable for model calibration and validation. A few test setup specific effects were identified which should be improved in future test campaigns. The three-point bending tests showed local indentation effects for profile sections of

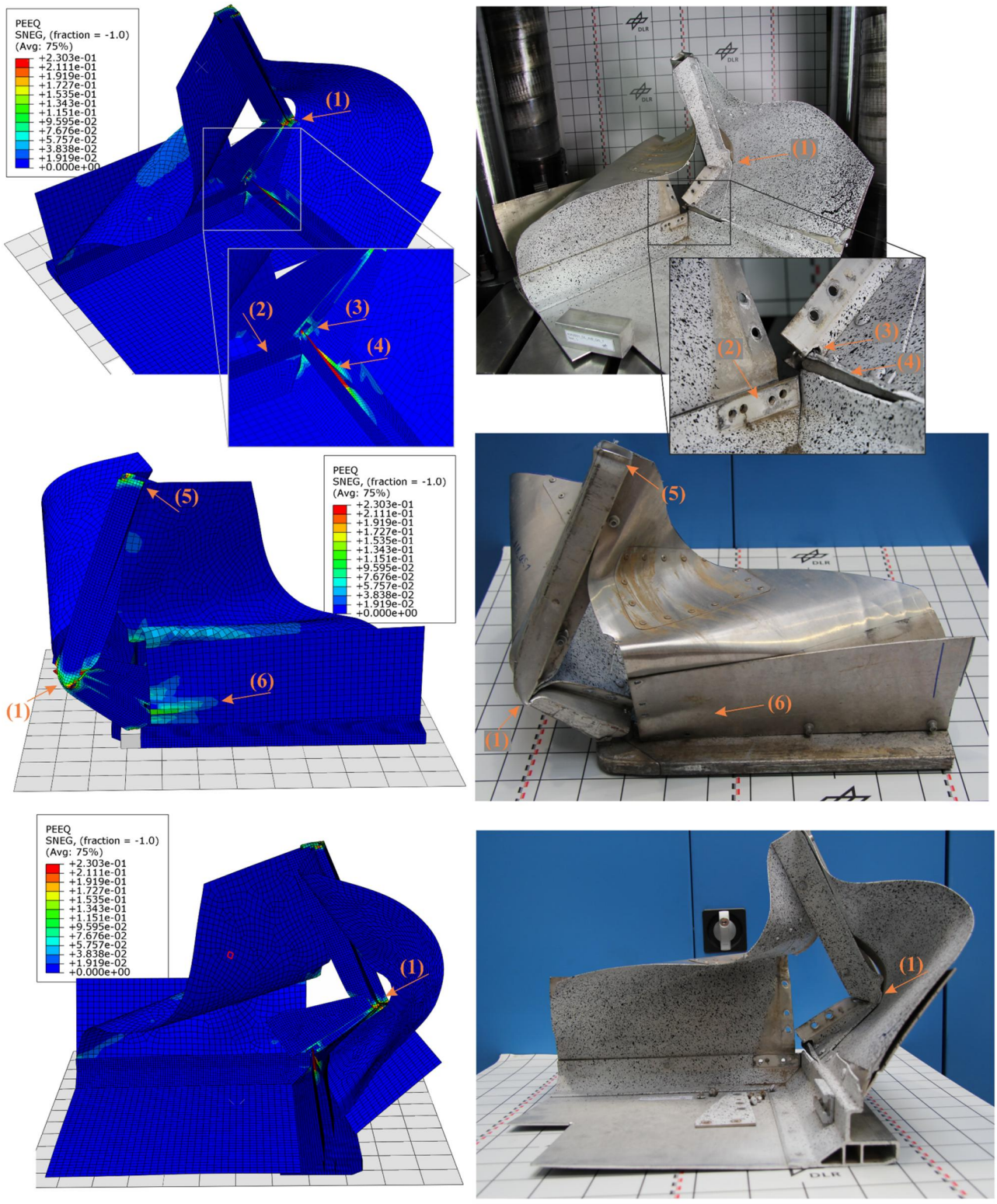

Figure 33. Base corner finite element simulation (contour plot of equivalent plastic strain) versus experiments, exemplarily shown for AIB base corner.

filigree design. Four point bending or other bending test set-ups might be a better solution. Clamping inserts installed for the roof corner tests partly interacted with the test specimen during testing. For future test campaigns, fixations and clamping inserts should consider all potential specimen deformations, also to a large extend. The full-scale test setup could be confirmed and provided good measurements, in particular for the force measurement without ringing or other falsifying effects in the signals.

As a secondary intent of this article, some aspects on the modelling of a container finite element model were presented with the focus on the most relevant parameters that

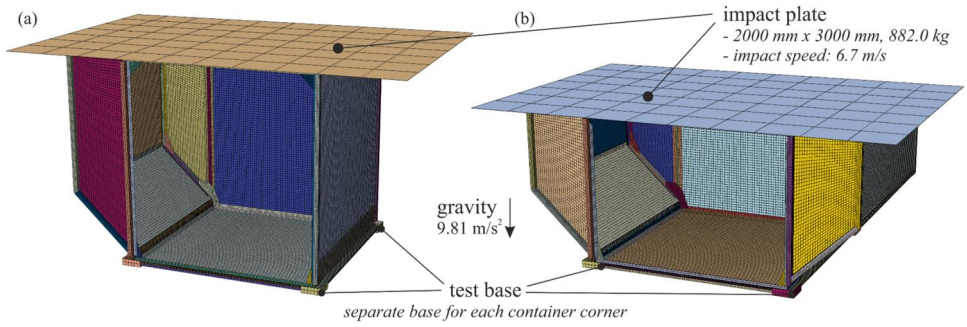

Figure 34. Finite element models of container full-scale test setups, (a) AKE container, (b) AKH container.

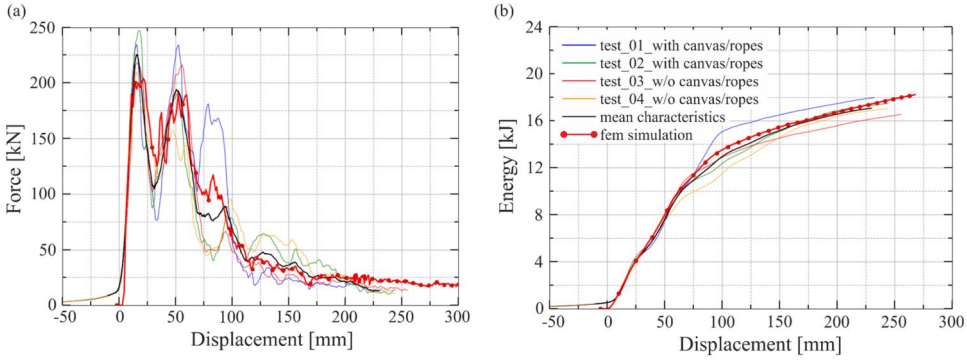

Figure 35. Force-displacement and energy-displacement results of simulation versus experiments for the AKE container.

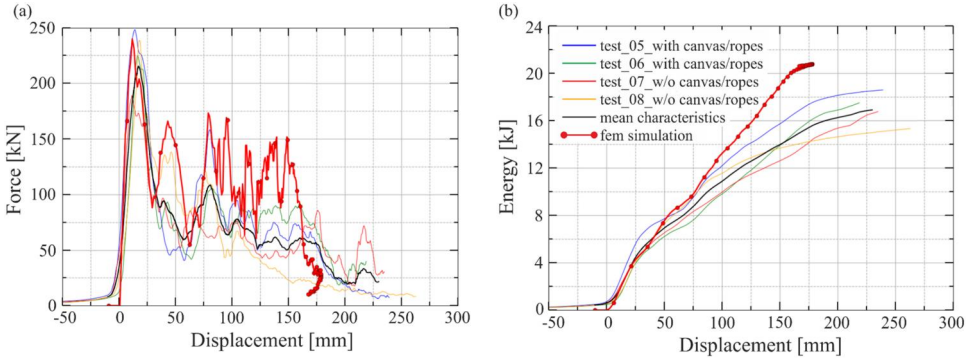

Figure 36. Force-displacement and energy-displacement results of simulation versus experiments for the AKH container.

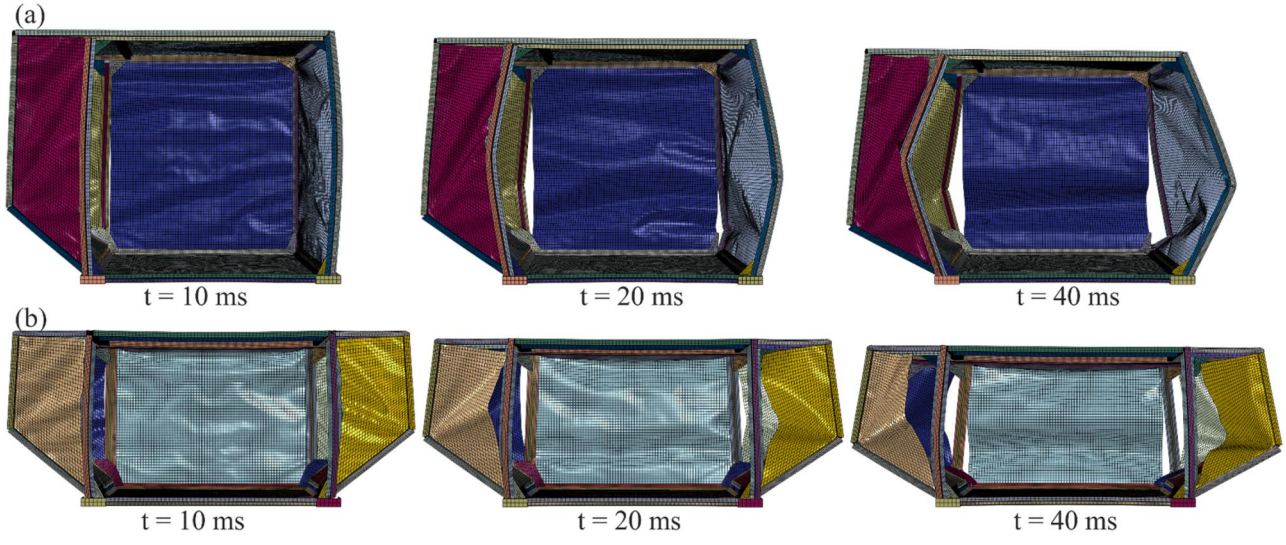

Figure 37. Crash sequences of full-scale simulations, (a) AKE container, (b) AKH container.

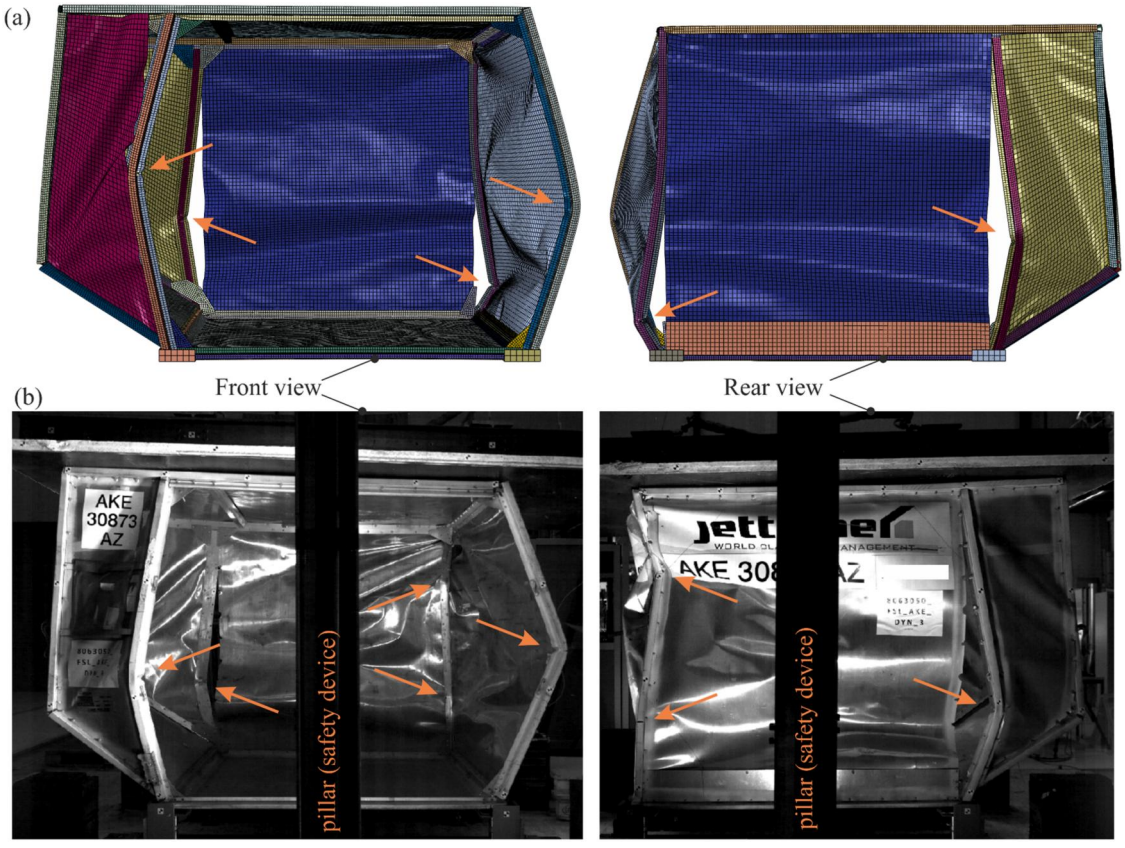

Figure 38. General failure kinematics of the AKE container with stanchion buckling, plastic hinge formation and sheet disintegration, (a) finite element simulation versus (b) experiment.

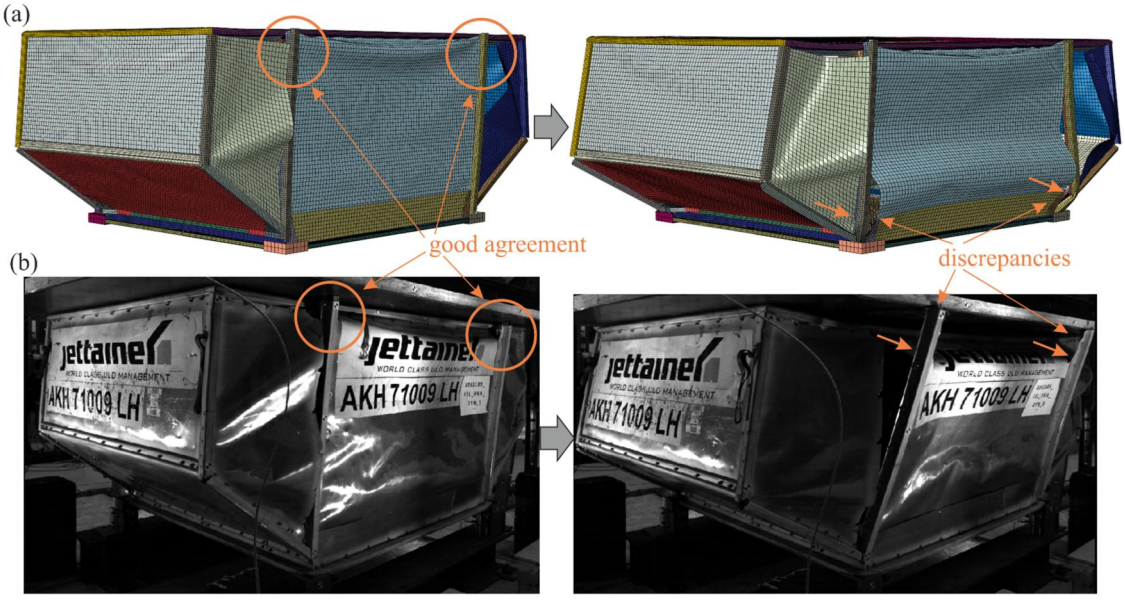

Figure 39. Rear stanchion failure kinematics of the AKH container with discrepancies in the simulation, (a) finite element simulation versus (b) experiment.

contribute to the container crash response. The element level tests were found to be suitable to select proper element sizes and to calibrate the material input for plastic hardening and damage based on the selected element size. The bolted joints modelling as well as the entire model assembly could be validated by the detail level tests. The fastener model as described in paragraph 4.2 could be confirmed. For double-lap or multi-lap bolted joints of the container assembly, it is recommended to define separate fastener models between the individual joint partners, as the primary

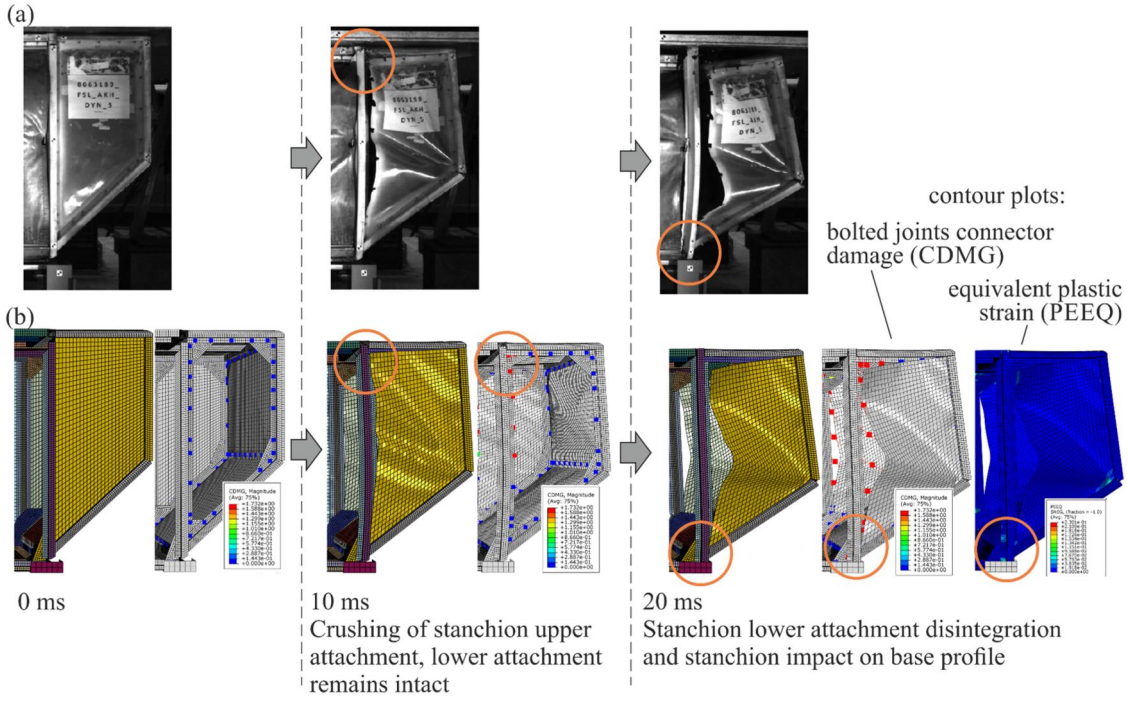

Figure 40. Detailed stanchion failure effects captured by the simulation, exemplarily shown for AKH container stanchion VR, (a) experiment versus (b) finite element simulation.

bolted joint failure mode is bearing failure. With that, bearing failure of multiple joining parts with significantly different part thickness, and hence different bearing strength, can correctly be modelled.

Compliance effects in the bolted assembly, due to large tolerances in the drill holes, were identified to play a major role in reaching the maximum load obtained in the base corner tests, as this compliance leads to parallel load paths through bolted joints and through contact interaction between stanchion and base profile. This effect could be captured well in the simulation based on initially made fastener stiffness assumptions. Proper stiffness input for the fastener models is expected to be crucial to capture this compliance effect. Optional bolted joint coupon testing, which at the end was not performed in the scope of this study, may end up in a large scatter due to this clearance effect.

Another challenge, in particular for the base corner simulations, was the existence of branching points where small details decided whether the base corner structure failed due to flange buckling, bolted joint failure or profile crushing, with significant influence on the total maximum force and the post-peak failure characteristics. On the other hand, the full-scale experiments showed good repeatability with fair agreement between the tests so that the effect of branching points was minor at the full-scale level.

With finalisation of this study, it remained an open question, how the cargo container is crushed in a real cargo compartment and whether the container stanchions are getting crushed or whether they punch through the cabin floor. The developed container finite element model will be capable to investigate this in the future by simulation.

Acknowledgements

The authors wish to thank Ulf Hartmann from Zodiac Aerospace and Janine Born from Jettainer for great support in purchasing the cargo containers and providing container design data.

Author contributions

Matthias Waimer: Conceptualisation, Methodology, Formal analysis, Investigation, Writing – original draft, Writing – review and editing. **Paul Schatrow:** Conceptualisation, Methodology, Formal analysis, Investigation, Writing – review and editing. **Tobias Behling:** Investigation, Writing – review and editing. **Dorothea Schlie:** Investigation, Writing – review and editing.

Disclosure statement

No potential conflict of interest was reported by the authors.

Funding

Parts of this work have received funding from the Clean Sky 2 Joint Undertaking under the European Union's Horizon 2020 research and innovation programme under grant agreement ID 807097.

ORCID

Matthias Waimer http://orcid.org/0000-0002-4899-6236
Paul Schatrow http://orcid.org/0000-0002-1341-5884
Tobias Behling http://orcid.org/0000-0001-6367-9557

References

[1] Abramowitz A, Smith TG, Vu T, et al. Vertical drop test of a narrow-body transport fuselage section with overhead stowage bins. DOT/FAA/AR-01/100; 2002.

[2] Logue TV, McGuire RJ, Reinhardt JW, et al. Vertical drop test of a narrow-body fuselage section with overhead stowage bins and auxiliary fuel tank on board. DOT/FAA/CT-94/116; 1995.
[3] Abramowitz A, Smith TG, Vu T. Vertical drop test of a narrow-body transport fuselage section with conformable auxiliary fuel tank onboard. DOT/FAA/AR-00/56; 2000.
[4] Jackson KE, Fasanella EL. Crash simulation of vertical drop tests of two Boeing 737 fuselage sections. DOT/FAA/AR-02/62; 2002.
[5] Littell JD. A summary of results from two full-scale Fokker F28 fuselage section drop tests. NASA/TM-2018-219829; 2018.
[6] Littell JD. A summary of airframe results from a Fokker F28 full-scale crash test. NASA/TM–2020-220572; 2020.
[7] Zhu S, Liu K, Xi X, et al. Influence of cargo luggage on the vertical drop crashworthiness of aircraft mid-fuselage section. Appl Sci. 2023;13(23):12921. doi: 10.3390/app132312921.
[8] Xianfei Z, Yunwen F, Xiaofeng X, et al. Evaluate the crashworthiness response of an aircraft fuselage section with luggage contained in the cargo hold. Int J Crashworthiness. 2017;22(4): 347–364. doi: 10.1080/13588265.2016.1258957.
[9] Arvin/Calspan: DC-10 fuselage drop test report, Arvin/Calspan report No. 72512, prepared for FAA technical center, Atlantic City, NJ; 1984.
[10] Rassian M. Virtual test & simulation, AIAA Complex Aerospace Systems Exchange (CASE) 2013. Los Angeles, California, USA, August 12–14; 2013.
[11] Zangani D, Ambrosetti S, Franitza P, et al. Development of a novel concept of explosion-resistant cargo container for narrow-body aircrafts. 27th International Congress of the Aeronautical Sciences ICAS 2010. International Council of the Aerospace Sciences, Nice, France, September 19–24; 2010.
[12] Hamm KR, Price DR, Imtiaz KS, et al. Revisiting building-block approaches for structures, SciTech Forum 2022; January 03–07; San Diego, CA, USA; 2022.
[13] International Organization for Standardization: road vehicles – objective rating metric for non-ambiguous signals. ISO/TS 18571; 2014.
[14] McGregor IJ. Impact performance of aluminium structures. In: Jones N, Wierzbicki T, editors. Structural crashworthiness and failure. London and New York: Elsevier Applied Science; 1993.
[15] Zukas JA, Nicholas TH, Swift HF, et al. Impact dynamics. New York: Wiley-Interscience Publication; 1982.
[16] Weyer S, Hooputra H, Zhou F. Modeling of self-piercing rivets using fasteners in crash analysis. ABAQUS User's Conference. 2006;
[17] Heimbs S, Schmeer S, Blaurock J, et al. Static and dynamic failure behaviour of bolted joints in carbon fibre composites. Composites Part A. 2013;47:91–101. doi: 10.1016/j.compositesa.2012.12.003.